SPECTROGRAPHIC TEMPERATURE MEASUREMENT OF A BREAKDOWN ARC WITHIN THE RIMFIRE GAS SWITCH

A Thesis
Presented to
The Faculty of the Graduate School
University of Missouri-Columbia

In Partial Fulfillment of the Requirements for the Degree
of Master of Science

By
CHRISTOPHER YECKEL

Dr. RANDY CURRY, Thesis Supervisor

JULY 2010

The undersigned, appointed by the Dean of the Graduate School, have examined the thesis entitled

SPECTROGRAPHIC TEMPERATURE MEASUREMENT OF A BREAKDOWN ARC WITHIN THE RIMFIRE GAS SWITCH

Presented by Christopher Yeckel

A candidate for the degree of Master of Science

and hereby certify that in their opinion it is worthy of acceptance.

_____

Dr. Randy Curry

_____

Dr. Thomas Clevenger

_____

Dr. Gregory Triplett

ACKNOWLEDGMENTS

The author would hereby like to whole-heartedly thank his advisor, Dr. Randy Curry for providing excellent guidance and support throughout the course of this work. Dr. Curry's patience and understanding are also greatly appreciated

The author thanks Sandia National Labs for their support.

The author thanks Andrew Benwell, Mark Kemp, Brian Hutsel, Jim Vangordon, Darren Swarts, and Dr. Robert Druce for their help and discussion.

The author thanks his parents, brothers, and the rest of his family for their positive support throughout his life.

Most of all, the author thanks his fiancé, Amy Vik, for her infinite patience and good humor during the long nights of making sure the graph was just right.

TABLE OF CONTENTS

LIST OF TABLES

LIST OF FIGURES

Chapter 1 Introduction

Gas switches are useful devices for transmitting large amounts of electrical energy in a short amount of time. Their ability to hold off high voltages and accommodate high current densities make them essential for many pulsed power systems. The RIMFIRE gas switch was developed by Sandia National Laboratories to transmit terawatts of power from the Marx store to the transmission line section. Sandia National Labs uses many RIMFIRE gas switches within its "Z-machine" accelerator to commute power from its 6-MV Marx generators for pulsed fusion experimentation. These RIMFIRE switches are triggered with laser pulses so that they all fire at precisely the same time.

There was a necessary interest in the physical processes involved with the generation of a plasma arc within the RIMFIRE gas switch. The motivation for these optical experiments is that the UV flux generated by the plasma may be depositing charge on the walls of the plastic insulator and contributing to an unacceptably high rate of switch failure due to insulator flashover. The photons emitted by the plasma can also be useful in characterizing the switch by identifying ejected electrode material, ionized background gases, and plasma temperature. This characterization could be useful in the development of gas switches with shorter rise times, higher power capabilities, and reduced failure rates.

Optically thick plasmas are found in gas switches when high current densities are present. High density plasma both emit and absorb photons which characterizes it as a black-body source. The black-body radiation emitted from the plasma has a maximum photon flux at

a certain wavelength, depending on the temperature. By using an optical multichannel analyzer (OMA) it is possible to find the wavelength of peak photon flux and consequently the temperature of the black-body source. The temperature can be useful in determining insulator material resistant to surface charge accumulation or UV damage. Spectral relative intensity measurements were obtained from the plasma arc in the gas switch by using fiber optics coupled into an OMA.

Determination of the temperature of the plasma can be useful when determining the causes of switch flashover. A high energy electron present at the triple point of the switch may travel across the insulator instead of the gap center due to the charge distribution on the insulator surface. The flashover event results in a reduction in the PMMA insulator's electrical insulating capabilities and the entire insulator must be replaced. This comes at a great cost in terms of time and money to installations such as Sandia National Laboratories where every shot costs thousands of dollars and delays cost millions. Minimizing the flashover rate will result in saved time and money.

This thesis explains the measurement of the temperature of high density plasma in a 3-MV switch using a fiber optic coupled to an OMA. The temperature of the plasma can then be used to determine the energy radiated per unit area per unit time. This information can then be used to develop insulator material resistant to the formation of surface charge due to incident UV light.

Chapter 2 Electrical Properties of the RIMFIRE Gas Switch Insulators

The reduction of the insulator flashover rate in the RIMFIRE gas switch is necessary for optimal accelerator operation. Replacing a damaged insulator is a time-consuming and expensive process in large systems such as Sandia National Lab's Z-Machine. Research into the prevention of flashover can save time and money by providing more reliable switch behavior. The RIMFIRE gas switch incorporates both solid and gas insulators in its trigger section [1].

The photons generated by the SF_6 breakdown arc during normal operation may be partially responsible for PMMA insulator flashover. High-intensity photons incident on the surface of the PMMA cause static charge accumulation through the photoelectric effect [2]. This static surface charge can cause localized electric field distortions across the insulator increasing the probability of a flashover event. Any spectrographic information regarding the incident photons may be useful in designing flashover-resistant switches. The temperature of the arc is of particular importance as it indicates the most intense wavelength energy of light incident on the insulator. By shifting the work function of the surface of the PMMA insulator away from the most intense photon wavelength, surface charge accumulation may be mitigated. Altering the PMMA surface chemically or by applying a coating could change the charging properties of the insulator while maintaining its dielectric strength.

Chapters two and three of this thesis discuss the electrical and optical characteristics, respectively, of the solid and gas insulators present in the trigger section of the RIMFIRE gas switch. A cutaway of Sandia's refurbished Z driver is shown in figure 2.1 [3]. The RIMFIRE laser triggered gas switch (LTGS) delivers power from the Marx bank into the pulse forming line. The timing of the trigger must be the same for every RIMFIRE switch in the system for optimal pulse delivery to the load.

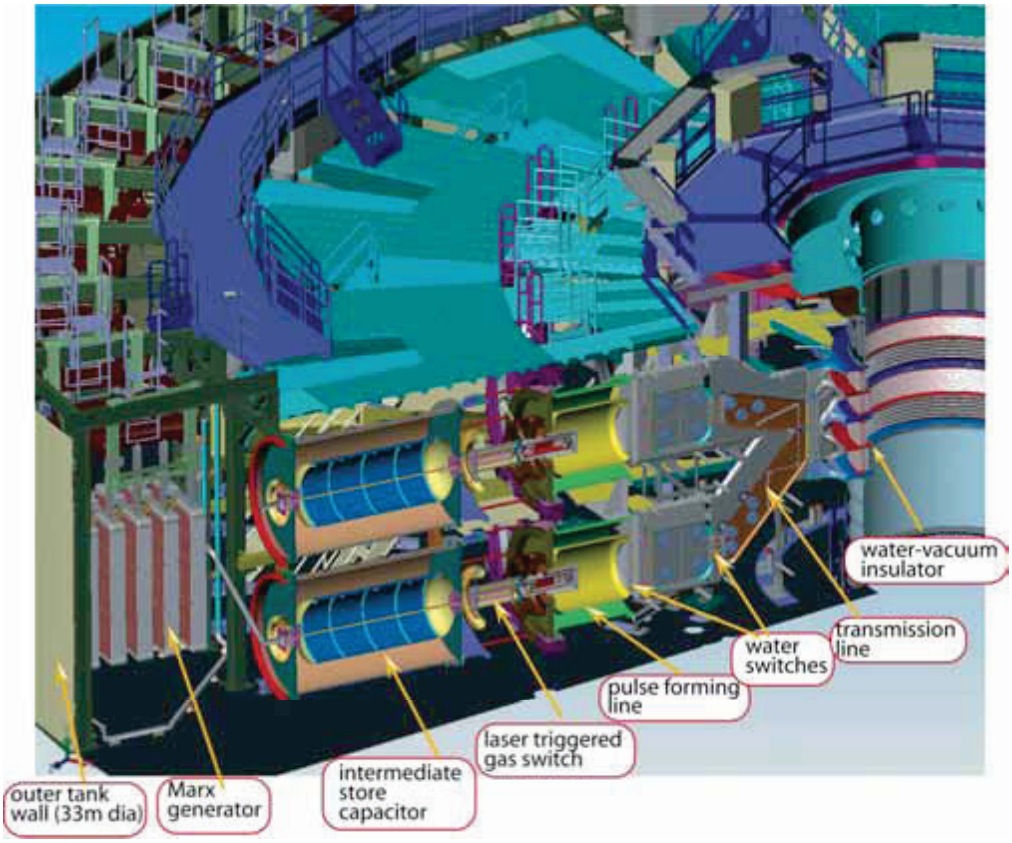

Figure 2.1. The refurbished Z driver has a 33-m diameter [3].

2.1 Properties of Dielectrics

Dielectric insulation is a vital part of any electrical system. Solid, liquid, and gas dielectrics are subjected to a variety of stresses over their lifetime and must be carefully considered in the design phase of the project to prevent system failure. The growing demand for high voltage electrical energy in the world today necessitates the constant improvement of dielectric insulation. The flashover of the PMMA insulator in the RIMFIRE gas switch is of primary concern as each failure is associated with several hours of costly refurbishment. Normally the breakdown event occurs between the two electrodes as an ionized channel through the insulating gas. In a flashover event, the arc forms across the surface of the insulator, causing conductive carbon tracking across the insulator and rendering its insulation capabilities useless [2,3]. The following sections discuss the mechanisms that lead to insulator flashover.

2.1.1 Coulomb's Law

Coulomb's Law is an equation describing the electrostatic force between two charges. Coulomb's Law is expressed by the equation

$$\boldsymbol{F} = \boldsymbol{qE} + \boldsymbol{q}(\boldsymbol{v} \times \boldsymbol{B}) \qquad [2.1]$$

The first term (*qE)* is a vector relation for a charge in an electric field. The second term is the Lorentz force on a moving charged particle in a magnetic field. The latter equation is a vector cross product, meaning that F is perpendicular to both the velocity vector and the magnetic field vector. Stray charges on the insulator surface may generate unwanted electric field distortions in accordance with equation 2.1.

2.1.2 Polarization and Dielectric Strength

Electrons in insulating dielectrics such as PMMA are not free to move as they are in conductors. Under an applied electric field a dielectric's inner electrostatics force the material to polarize into dipoles [5]. The maximum electrical stress that a dielectric's polarized dipoles can withstand is known as its dielectric breakdown strength. The dielectric breakdown strength is defined as the maximum value of applied electric field at which a dielectric material, stressed in a homogenous field electrode system, breaks down and loses its insulating property. The damage is caused by an ionized channel (arc) that punches a permanent hole through the insulator. The dielectric strength is given in units of V/m. The PMMA has a dielectric strength of 25-MV/m [6]. Factors such as material purity, time of applied field, electrode geometry, and other environmental parameters characterize a material's dielectric strength [7]. Figure 2.2 shows dipoles that were formed by electrostatic polarization in the presence of an applied electric field. Unlike a liquid or gas, these non-neutral charges are embedded.

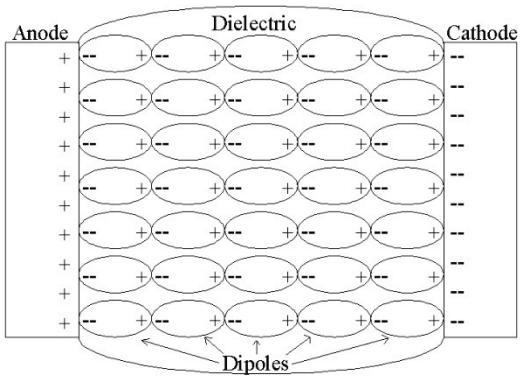

Figure 2.2. The application of an electric field to a dielectric forces the molecules in the material to polarize and align. The electric field points from left to right.

2.2 Dielectric Materials

Dielectric materials can be divided into three subcategories: gases, liquids, and solids. All dielectrics, except a perfect vacuum, conduct charge in an applied electric field. These three dielectric forms, exhibit varying characteristics. The RIMFIRE gas switch incorporates both gas and solid dielectrics. The solid dielectric is a transparent polymer known as Poly(methyl methacrylate) (PMMA). The gas dielectric is SF_6 gas and is well known for its insulating and breakdown recovery properties.

2.2.1 Gas Dielectrics

The molecules in the SF_6 gas do not interact in a significant way since there are no bonds linking them. Since the electrons that make up a gas molecule are tightly bound in discrete energy levels no net charge can pass through unless the system is disturbed. Charge is passed through a gas through local interactions of electrons, ions, and charged particles. A gas dielectric will break down at a certain electrical stress depending on pressure and temperature [8].

Utilizing Boyle's law and Gay Lussac's law we obtain the ideal gas law

$$\boldsymbol{PV = nRT} \qquad [2.5]$$

where P is the pressure, V is the volume, n is the number of moles, T is the temperature of the gas, and R is the universal gas constant. The ideal gas law can be applied to any gas dielectric. The kinetic energy of the gas can be related to its thermal energy by

$$\boldsymbol{\frac{1}{2}mv^2 = \frac{3}{2}kT} \qquad [2.6]$$

where **υ** is the molecular velocity, **m** is the mass, and k is the Boltzmann constant is equal to 1.381×10^{-23} K. Gas molecules will have a Maxwell distribution of velocities ranging from zero to infinity in the absence of an electric field [8].

These gas molecules collide with each other on a regular basis. Since the motion is Maxwellian, an average time between collisions and a collisional cross-section can be calculated. The mean free path of the particles differs greatly depending on the size and number of particles. If there are $\mathbf{N_p}$ pairs of particles of radii $\mathbf{r_1}$ and $\mathbf{r_2}$ then the mean free path is

$$\bar{\lambda} = \frac{1}{\pi (r_1 + r_2)^2 N_p} = \frac{1}{\delta} \qquad [2.7]$$

where **δ** is the effective collision cross-section. The gas breaks down electrically due to the generation and collision of charged particles accelerated in an electric field. These charged particles are formed by electric fields in the bulk of the gas and charge emission from the electrodes [9].

2.2.2 Solid Dielectrics

Compared to most liquids and gases, solids have a higher dielectric strength. Solids are composed of many different atomic structures. The PMMA, in particular, is an acrylic molding resin [6]. Acrylic molding compounds have superlative optical properties and weatherability. Acrylics are produced by polymerizing methyl methacrylate alone or combined with other unsaturated polymers [6]. The chemical formula of PMMA is illustrated in figure 2.3.

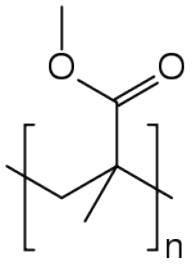

Figure 2.3. The chemical formula for the PMMA acrylic repeating unit is $(C_5O_2H_8)_n$.

The polymer PMMA is also widely used for its excellent electrical properties. Acrylic resins exhibit outstanding arc resistance making them useful in high voltage applications. The dielectric constant of PMMA decreases with increasing electrical frequency [6].

2.2.3 Liquid Dielectrics

Dielectric liquids used in electrical systems tend to consist of covalently bonded molecules that are relatively non-polar. The four types of liquid dielectrics are non-polar, mildly polar, strongly polar but not associated, and strongly polar and associated. Examples of these types are transformer oil, chlorinated diphenyl, propylene carbonate, and water, respectively [5]. A liquid with a high dielectric strength may be useful as a coating to modify the work function of the insulator surface.

The main concern with liquid dielectrics are their susceptibility to conducting impurities. Macroscopic charge carriers can act as field enhancements and trigger breakdown due to localized electrical field enhancement. This results in the creation of other charge carriers and leads to avalanche breakdown [6]. The RIMFIRE gas switch does not incorporate any liquid dielectrics so no further consideration will be given to them in this thesis.

2.3 Gas Breakdown Theory

Electric field breakdown in a gas is initiated by electron emission from the cathode. The generated space charge distribution near the cathode surface affects all local charge carriers [10]. All dielectric media maintain their highest breakdown strength in a homogenous electric field. With increasing field inhomogeneity the breakdown strength decreases due to the development of regions of higher electrical breakdown. In figure 2.4 the plane-plane electrode gap configuration has higher breakdown field strength than the point-point electrode gap configuration due to a phenomenon known as field enhancement.

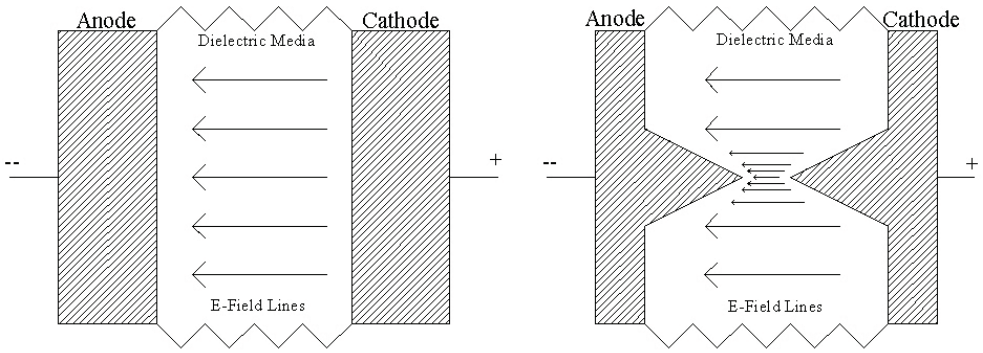

Figure 2.4. The plane-plane configuration has higher breakdown strength than the point-point configuration due to a homogenous electric field.

It is important to note that the RIMFIRE gas switch is designed so that there is minimal field enhancement across the gap. The only significant field enhancement can be found at the triple points, which will be discussed in a later section. Field enhancement at the triple point has a role in all flashover events [11]. Figure 2.5 was taken from a paper by Sudarshan [11] which illustrates some flashover initiating events in a gas.

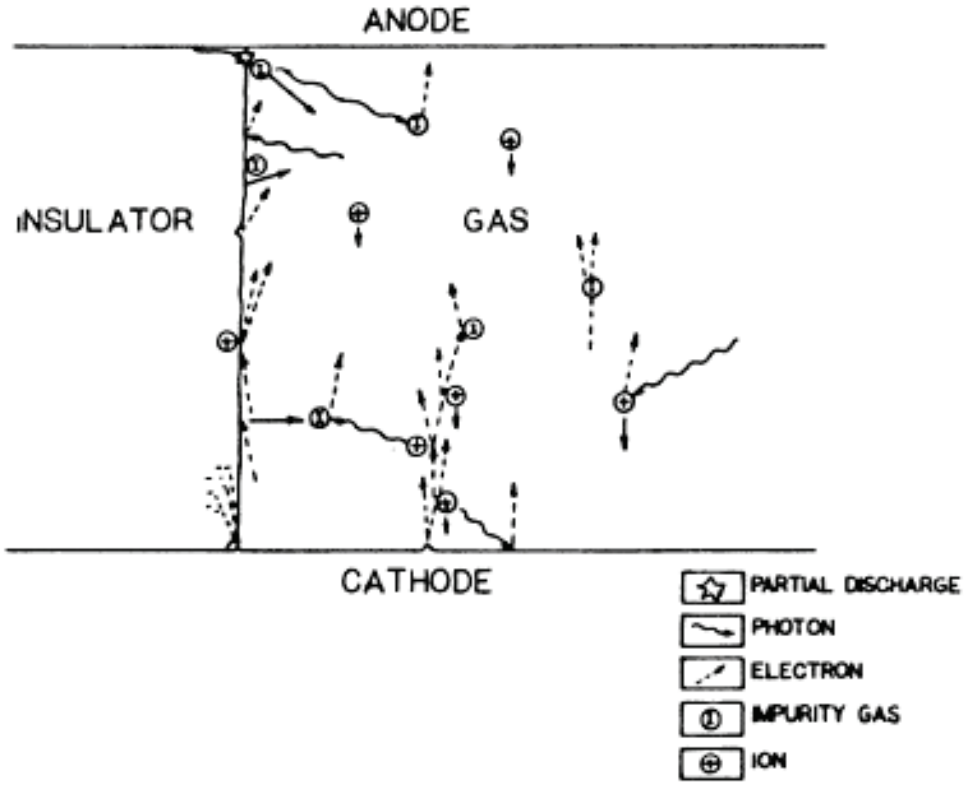

Figure 2.5. Illustration of some of the processes that may play an important role in insulator flashover in gases [11].

2.3.1 Breakdown in SF_6 Gas

The RIMFIRE switch is filled with SF_6 gas as a switching medium. The SF_6 is an electronegative gas with high breakdown strength and good chemical stability. The physical properties of SF_6 are listed in table 2.1. The pressure of the SF_6 in the RIMFIRE was maintained at 30-psig for all of the tests performed.

Table 2.1. This table lists the physical properties of SF_6 gas. SF_6 is used as the breakdown medium in the RIMFIRE gas switch [12].

Physical Properties of SF_6	
Molecular Weight	146.6
Melting Point	-50.8°C
Liquid Density at 25°C	1.33 g/ml
Gas Density at 1 bar at 20°C	6.2 g/l
Relative Density	5.1
Critical Density	0.735 g/ml
Critical Temperature	45.6°C
Boiling Point	-63.0°C
Sublimation Temperature	-63.9°C
Critical Pressure	35.56 bar
Specific Heat at 30°C	0.559 J/g
Thermal Conductivity	0.1407 W/m°C
Dielectric Constant	1-1.07
Vapor Pressure at 20°C	10.62 bar

The SF_6 gas will undergo decomposition and oxidation in an electrical discharge. When SF_6 is dissociated in an electrical discharge, the products tend to recombine at a rapid rate to reform SF_6 restoring the original dielectric strength [12]. This makes SF_6 a reliable switching medium. The SF_6 has better heat dissipation and four times the convective cooling efficiency of air [5]. The SF_6 molecule is illustrated in figure 2.6.

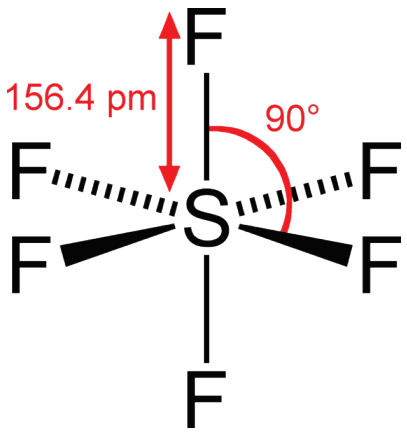

Figure 2.6. The SF_6 molecule has an octahedral geometry with a much higher density than air.

2.3.2 Generation of Charged Particles

For a current to flow between the electrodes in a gas there must be charged particles present in the gas. These particles include electrons, positive ions, and negative ions. The generation of free electrons can result from the ionization of neutral atoms or from detachment of negative ions.

There are four types of ionization reactions. *Ionization by collision*, also known as impact ionization, occurs when a free electron either elastically or inelastically collides with a neutral gas molecule. In the case of an inelastic collision the gas molecule becomes ionized and a positive ion and an extra electron are produced. An electron excited to a higher energy state due to a photon impact is known as *photoionization* [9]. Photoionization can be produced internally by photons released by electrons dropping to a lower energy state or externally by sources such as breakdown arcs. *Thermal ionization* occurs as the temperature of a gas increases the gas particle collision rate. *Electron detachment* occurs when an electron detaches from a negative ion. In this process slow moving negative ions are converted to fast-moving electrons [9]. These electrons are more effective at generating further ionization than the parent negative ion. Table 2.2 lists some possible reactions that lead to breakdown in electronegative SF_6 gas [13].

Table 2.2. Some possible reactions in SF_6 leading to breakdown [9,13].

$SF_6 + e$	$SF_4 + 2F + e$
$SF_6 + e$	$SF_2 + 4F + e$
$SF_6 + e$	$SF_5 + F + e$
$SF_5 + SF_5$	S_2F_{10}
$SF_4 + H_2O$	$SOF_2 + 2HF$
$SF_4 + O$	SOF_4
$SOF_2 + H_2O$	$SO_2 + 2HF$

There are four more types of ionization reactions that occur at the electrode surfaces, particularly the cathode. Normally the electrons are bound to the surface of the cathode, but given enough energy they can be emitted into the gas [14]. *Ion bombardment* of the cathode can release two electrons given that the energy of the ion is twice the cathode work function. The first electron neutralizes the ion and the second is released into the gas to create more ionization reactions. If a photon with energy greater than the work function of the cathode strikes the cathode, an electron can be released in a process known as *photoemission*. Raising the temperature of the cathode to a very high value will create intense lattice vibrations. These vibrations lower the work function of the metal allowing the lower energy electron to escape the cathode known as *thermionic emission*. *Field emission* results from a high electrostatic field that overcomes the binding force between electrons and protons which leads to the emission of electrons from the cathode surface. This process requires fields in excess of 10^7-10^9 V/m [15]. All four emission mechanisms contribute in a typical discharge [11].

2.3.3 Reduction of Charged Particles

While the processes described above involve the generation of charged particles to aid in the breakdown phenomenon, there are also many similar processes that remove charged particles and inhibit breakdown. *Positive-negative ion recombination* is a type of charge transfer where a positive and a negative ion collide to form a neutral ion structure [16].

Typically, the processes that remove charge from a particle are the opposite processes that add charge to a particle. These recombination reactions dominate after the collapse of

an arc channel. The SF_6 is well-known for its ability to recombine quickly after a discharge. Recombination is necessary in order for a gas to achieve its pre-discharge breakdown strength [18]. The recombination neutralizes the charged particles in the gas limiting the particle drift in the subsequent applied electric field.

2.3.4 Townsend Theory of Breakdown

A gas is normally an almost perfect insulator. The primary ionization processes in the SF_6 gas are initiated by electron/gas molecule collision and are represented by the Townsend first ionization coefficient **α** in equation 2.11,

$$\boldsymbol{\gamma[\exp(\alpha d) - 1] = 1} \qquad [2.11]$$

where **d** is the gap spacing and **γ** is the Townsend second ionization coefficient which is defined as the net number of secondary electrons produced per primary electron leaving the cathode. The Townsend ionization coefficient **γ** is a function of electric field over pressure (E/P) and the material. The first ionization coefficient **α** is defined as the number of ionizing collisions by an electron per unit distance as it travels in the direction of the applied field [18].

Breakdown results if the equation is greater than unity. The distinguishing feature of a Townsend discharge is that the space charge of a single avalanche does not distort the electric field in the gap. This initial discharge leads to streamer and avalanche breakdown [18].

Streamer and avalanche breakdowns involve the interaction of the electric field generated by the breakdown and the ambient electric field. The space charge of an avalanche can transform the avalanche into a plasma streamer. Photons generated from the avalanche can further excite photoelectrons and generate more impact ionization collisions. This can generate a scenario where multiple avalanches develop and propagate across the gap. Typically, streamer discharges occur at high pressures and gap lengths [5].

2.4 Cathode Electron Emission and Gas Breakdown Probability

An important role in SF_6 gas breakdown and insulator flashover is the field emission from cathode surface defects. These surface imperfections include microprotrusions, dielectric inclusions, oxide, and other inorganic dielectric films, adsorbed gas layers, grain boundaries at the surface, micro particles, oil vapor cracking products, craters formed at the electrode surface, pores, and cracks. These flaws become electron emission centers which participate in primary or secondary processes leading to gas breakdown [8,9].

2.4.1 Cathode Electron Emission

The field emission from the cathode is a result of the tunneling of electrons through the potential barrier at the metal-gas interface due to a strong electric field. This phenomenon leads to the field emission theory known as the Fowler-Nordheim equation. The equation is

$$\boldsymbol{I(E_{surf}) = \frac{A_{FN}(\beta E_{surf})^2}{\varphi} \exp\left(-\frac{B_{FN}\varphi^{\frac{3}{2}}}{\beta E_{surf}}\right)} \quad [2.8]$$

where $E=\beta E_{surf}$, $I(E_{surf})$ is the field emission current density (A/cm^2), E_{surf} is the electric field (MV/m), φ is the work function of the metal (eV), and A_{FN} and B_{FN} are constants. The β term is the ratio of the local electric field to the average surface field [6,7]. The Fowler-Nordheim equation is useful for analysis of cathode emission in gas dielectrics [8,9,10].

2.4.2 Breakdown Probability in a Gas Switch

Predicting the probability of a breakdown occurrence is vital to designing gas switches. Nitta *et. al.* proposed a breakdown probability function derived from an extreme-value distribution of the form [8],

$$\boldsymbol{P(A) = 1 - \exp\{-\lambda A\left(\frac{E - E_0}{E_d}\right)^m\}}$$

where *P(A)* is the cumulative probability of breakdown, *A* is the electrode area, for which the breakdown field is *E,* and E_d is the theoretical breakdown field. E_0 is the minimum breakdown field for very large electrode area at a particular pressure, dependent only on the gas and pressure. λ is a constant dependent on the gas, surface roughness and pressure and *m* is a constant dependent on the gas, but independent of pressure or surface roughness, being equal to 7.4 for SF_6 [6].

2.4.3 Field Enhancement Factors

The field emission current from the imperfections on the cathode surface helps initiate breakdown in a gas across the gap and insulator surface. This field emission current is increased by field enhancement at the tips of the cathode protrusions. This enhancement is known as the field enhancement factor β_E. The field enhancement factor is defined as

the ratio of the actual electric field at the tip of the protrusion to the average macroscopic field [19]. The enhancement can be approximated by the height of the protrusion divided by the radius of curvature. The field enhancement of these protrusions increases with decreasing radius of curvature. The electric field at the tips of the cathode protrusions is given by

$$E_{c0} = \frac{E_c h}{r_c} = \beta_E E_c \qquad [2.11]$$

where E_c is the field strength of the gap, E_{c0} is the enhanced electric field, h is the protrusion height, r is the protrusion radius of curvature, and β_E is the field enhancement factor [19].

While the imperfections on the cathode surface are normally undesirable, many electrode geometries incorporate field enhancements in order to trigger specific breakdown phenomenon. Sphere-sphere, point-point (as in figure 2.4), plane-point, sphere-plane, etc all have benefits and disadvantages. A point-point electrode geometry will ensure that the breakdown occurs only at the cathode tip, however, the point is more prone to damage due to localized heating which limits its lifetime. A plane-plane geometry has increased lifetime but more spatially unpredictable breakdown behavior [19].

The other mechanism that initiates an arc in a gas is through the charging of dielectric films and inclusions by the current of the plasma ions, followed by the breakdown of these films. In this case, the density of the breakdown-initiating plasma is lower than the field enhancement case by several orders of magnitude [20].

2.4.4 Generation of a Field Enhancement

Explosive electron emission is the thermo-electron emission from cathode regions heated to high temperatures due to micro-explosions [21]. An electric arc will be emitted from the zone of the explosion during an electrical discharge at the cathode. The discharge arc generates very high temperatures which are much higher than the critical point temperature of the cathode material causing melting and sputtering. This phenomenon can be explained by the Richardson-Schottky formula

$$j = AT^2 exp(-\frac{e\varphi - \alpha E^{\frac{1}{2}}}{kT}) \qquad [2.12]$$

where **A**=120.4; **α**=3.79x10^{-4}, **φ** is the work function of the cathode, **k** is Boltzmann's constant, **E** is the electric field at the emitting surface (V/cm), **T** is the cathode temperature (K), and **j** is the electron current density (A/cm^2). Figure 2.7 shows the geometry of an explosive emission center on a point and plane configuration [21].

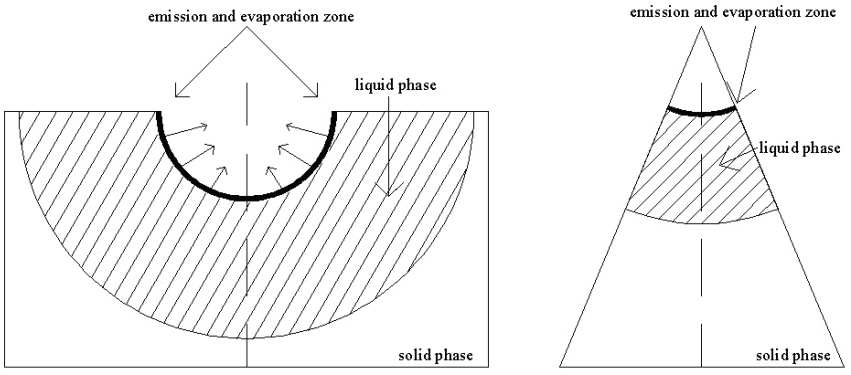

Figure 2.7. Emission center geometry on tip of a point cathode and on the surface of a plane cathode [21]

A small volume of the cathode is heated quickly until it explodes. As the explosion develops the emission zone increases in size and heat is removed by conduction,

evaporation, and ejection of the heated liquid metal. This reduces the temperature and thermo-electron emission current density in this zone leading to intense cooling. The explosive emission current ceases and a crater is generated. A flashover event may cause a crater to develop near the triple point increasing the probability of a subsequent flashover [21].

2.4.5 Triple Point Enhancement

Where three types of material come together is known as the triple point. In the case of the RIMFIRE gas switch these three media are the stainless steel electrodes, plastic insulator (PMMA), and SF_6 gas. Electric fields at a triple point can be enhanced by ten times or more [2,11]. Most flashover events are initiated by the high fields at the triple point. At the metal-dielectric boundary, the microscopic surfaces are rough so they touch one another only by their protrusions [11]. These protrusions act as field enhancements which cause intense localized electron emission.

The bombardment of electrons on the surface of the dielectric from the cathode protrusions at the triple point can charge up the surface of the solid insulating dielectric. Charging the insulator surface generates a voltage gradient across the insulator between the cathode and the anode [2]. It also leads to the appearance of undesirable gas in the gap due to gas desorption from the insulator. A flashover can result if the charges generated on the insulator surface by the incident photons and the triple point form a path for the electrons to travel [2].

2.5 Insulator Flashover

Electrons emitted at the triple junction and photons emitted from the breakdown arc create an undesirable charge accumulation across the insulator surface. The appearance of a non-neutral charge at the dielectric surface gives rise to a redistribution of the voltage potential over the insulator length. A flashover event occurs when electrons find charge conditions along the insulator surface favorable for avalanche breakdown. Chapter 3 goes into depth on the formation of surface charge due to incident photon flux from the arc in a high voltage switch.

References for Chapter 2

[1] S. Rosenthal, J. Elizondo, J. Maenchen, K. Struve, "Modeling 6-MV Gas Switches for the ZR Accelerator", IEEE, 2003.

[2] T. Nitta, Y. Shibuya, Y. Fujiwara, Y. Arahata, H. Takahashi, H. Kuwahara, "Factors Controlling Surface Flashover in SF_6 Gas Insulated Systems", IEEE Trans. on Power App. and Sys., 1978.

[3] G. Iyer, R. Corur, "Prediction of Electrical Performance of Medium Voltage Epoxy Insulated Equipment", IEEE, 2010.

[4] K.LeChien, M. Savage, V. Anaya, D. Bliss, et all., "Development of a 5.4 MV Laser Triggered Gas Switch for Multimodule, Multimegampere Pulsed Power Drivers", Phys. Rev. Special Topics, 2008.

[5] P.J. Harrop, *Dielectrics*, John Wiley, New York, 1972.

[6] W.T Shugg, *Handbook of Electrical and Electronic Insulating Materials*, IEEE Press, Piscataway, NJ, 1995.

[7] H.H. Malik, A.A. Al-Arainy, M.I. Qureshi, *Electrical Insulation in Power Systems*, Marcel Dekker, New York, 1998.

[8] J.C. Martin, *On Pulsed Power*, Plenum Press, New York, 1996.

[9] M.A. Lieberman, *Principles of Plasma Discharges and Materials Processing*, Wiley, Hoboken, New Jersey, 2005.

[10] H. Blume, *Pulsed Power Systems*, Springer, Germany, 2006.

[11] T. Sudarshan, R. Dougal, "Mechanisms of Surface Flashover Along Solid Dielectrics In Compressed Gasses: A Review", IEE Trans. Elec. Insul. 1986.

[12] V.Y. Ushakov, *Insulation of High-Voltage Equipment*, Springer, New York, 2004.

[13] I. Sauers, "Sensitive Detection of By-Products Formed in Electrically Discharged Sulfur Hexafluoride," IEEE Trans. of Elec. Insul. Vol. EI-21 No.2, April 1986.

[14] R.H Fowler and L.Nordheim, "Electron Emission in Intense Electric Fields", in Proc. Roy. Soc., London, A119. pp. 173-181, 1928.

[15] M. BastaniNejad, A. A. Elmustafa, "Evidence for Fowler-Nordheim Behavior in RF Breakdown," Proceedings of PAC07, Albuquerque, New Mexico, USA.

[16] R. Morrow, "A Survey of the Electron and Ion Transport Properties of SF_6", IEEE Trans. on Plasma Sci., 1986.

[17] S. Garanin and E. Palagina, "Evaluation of the Ionization and Recombination Processes in Low-Density Plasma Based on the Statistical Model of an Atom", IEEE Conf. on Plasma Sci., 2007.

[18] A. Cookson, "Review of High-Voltage Gas Breakdown and Insulators in Compressed Gasses," IEEE Proc., vol 128, Pt. A, no. 4, 1981.

[19] G. A. Mesyats, *Pulsed Power*, Kluwer Academic, New York, 2005.

[20] E. L. Murphy and R. H. Good, "Thermionic Emission, Field Emission and the Transition Region", Physical Review, Vol. 102, No. 6, 1956.

[21] G.A. Mesyats, "Ecton or Electron Avalanche from Metal", IOPScience, Physics –Uspekhi, 38 (6) 567 – 591, 1995.

[22] E. Husain and R. Nima, "Analysis of Paschen Curves for Air, N_2, and SF_6 Using the Townsend Breakdown Equation", IEEE Trans. on Elec. Insul., 1982.

Chapter 3 Optical Properties of the RIMFIRE Gas Switch Insulators

3.1 Optical Properties of PMMA

Every atom is comprised of negatively charged electrons orbiting a positively charged nucleus in discrete energy orbits. The electrons in the outermost orbital shell are known as valence electrons and are responsible for all atomic bonding processes. It is possible for an electron in this band to gain enough energy to free itself from the nucleus and become a free carrier in the conduction band. This energy separation, or work function, between the valence band and the conduction band of an atom is known as its band gap. The band gap is a measure of the amount of energy an electron must gain within an atomic lattice to become a free-carrier. In an insulator, this energy separation is large while in a conductor this energy separation may be negligible or zero [1]. Figure 3.1 illustrates the band gap concept.

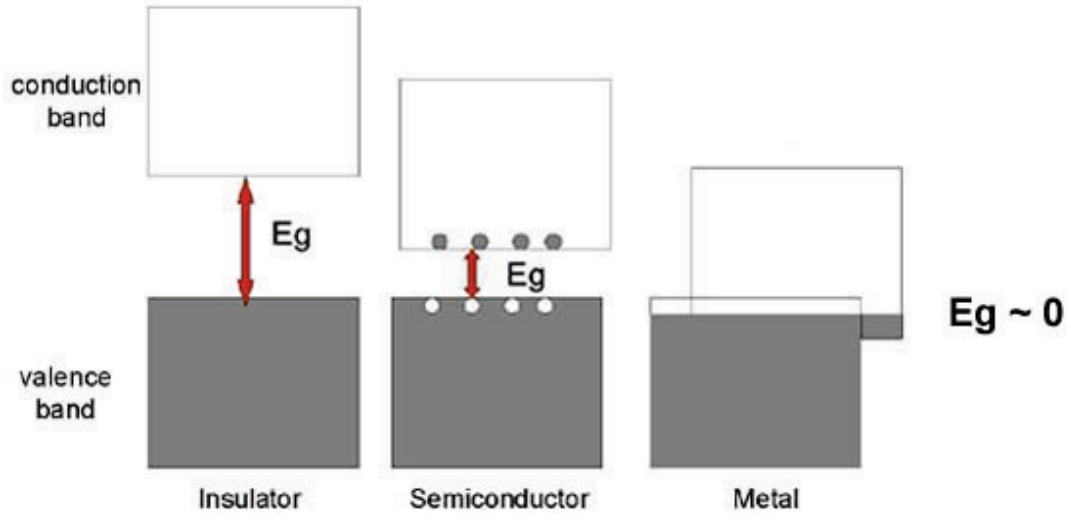

Figure 3.1 This figure illustrates the band gap in an insulator, semiconductor, and metal. The larger the separation of the bands the more energy needed to shift an electron from the valence band into the conduction band.

The UV photons generated by the plasma arc in the RIMFIRE gas switch are thought to strike the PMMA insulator surface imparting energy to the bound electrons through the photoionization processes described in chapter 2. This electron energy gain shifts the electrons from the valence band up into the conduction band of the PMMA causing them to become free carriers. Once enough electrons are established as free carriers they can form charge gradients across the surface of the insulator which may lead to flashover [2,3]. The photon flux at each wavelength of light can be determined though spectrographic analysis. A large amount of photon flux at a specific wavelength may generate large concentrations of free carriers on the surface of the PMMA insulator. This chapter explains the physics of this phenomenon.

The band gap energy of PMMA is between 5.75 and 6.07-eV [4]. The photon wavelength corresponding to this band gap energy is given by:

$$E_{gap} = hv = \frac{hc}{\lambda_{photon}} \qquad [3.1]$$

where E_{gap} is the energy of the band gap of PMMA, h is plank's constant, v is the photon frequency, λ_{photon} is the wavelength of the photon, and c is the speed of light in a vacuum. A band gap energy of 5.75-eV corresponds to a photon wavelength of 215.6-nm. However, impurities in the PMMA can cause band gap inconsistencies allowing photons from many wavelengths to create free carriers [5]. This multiphoton ionization process can result in surface charging. Every material has several minor band gaps that can also be used for the creation of free carriers [1].

3.1.1 Discrete Electron Energy Band Theory

A bound electron can only exist in discrete energy orbits. This section is a brief mathematical overview of how these discrete energy bands arise in materials. The band gap of any material can be derived using the Bloch Theorem coupled with the Kronig-Penny Model. Energy bands in a material arise naturally from the allowed energy states of an electron oscillating in a periodic potential. The Bloch Theorem is used in quantum mechanics to relate the value of the wave function within a "unit cell" of a periodic structure to any other point in the structure. Using Schrodinger's Wave Function for example, **if** U(x) is periodic such that U(x+a) = U(x), **then** $\Psi(x+a) = e^{ika}\,\Psi(x)$. Details concerning Schrodinger's Wave Function are not covered in this thesis but can be found in Pierret[1].

The Bloch Theorem is used to derive the Kronig-Penny Model. This model is the idealization of the actual material's periodic potential. The Kronig-Penny Model involves a mathematical derivation which uses the Bloch Theorem and boundary conditions to solve the differential wave function. The boundary conditions are the continuity and periodicity requirements of the material. Solutions for the Kronig-Penney Model can be obtained in the form:

$$F(E) = \cos(kL) \qquad [3.2]$$

where for -Vo < E < 0,

$$F(E) = \cos(\alpha(L-b))\cosh\beta b - \frac{\alpha^2-\beta^2}{2\alpha\beta}\sin(\alpha(L-b))\sinh\beta b$$

and for E> 0,

$$F(E) = \cos(\alpha(L-b))\cos kb - \frac{\alpha^2 + k^2}{2\alpha k}\sin(\alpha(L-b))\sin kb \qquad [3.3]$$

L and *b* are constants associated with the crystal lattice and

$$k = \sqrt{\frac{2mE}{\hbar^2}}$$

$$\alpha = \sqrt{\frac{2m(|V_0| + E)}{\hbar^2}}$$

$$\beta = \sqrt{-\frac{2m|E|}{\hbar^2}} \qquad [3.4]$$

The value of ***k*** can be a continuum of values because the crystal is assumed to be infinite. Therefore, $\cos(kL)$ can be any value in the range of cosine (i.e. $-1 \leq \cos(kL) \leq 1$) The allowed electron energies can then be found for finding values of F(E) that satisfy $|F(E)| \leq 1$.

The Kronig-Penny Model shows that there are limited levels of allowed discrete energies bordered by discrete forbidden energies where electrons cannot exist. The ranges of allowed energies are called energy bands and the ranges of forbidden energies are called band gaps. These band gaps play an important role in the spectroscopic analysis of plasma as they determine the photon emission and absorption characteristics [1,7]. A photon incident on surface of a material that is the same energy as the band gap of the material will lose its energy to the electron and the electron will shift across the band gap into the next highest energy band.

3.1.2 Photon Emission

The energy required to energize an electron to a higher energy state across a band gap comes from the collision mechanisms outlined in chapter 2. *Photoionization* is a phenomenon that results in an energy transfer between a photon and an electron. When a photon strikes an electron, the photon energy is added to the electron energy and the photon ceases to exist. The energy of the photon is given by equation 3.1. The incident photons interact with both the SF_6 gas and the PMMA insulator forcing them to absorb and emit photons based on their respective band gaps. It also results in the formation of free carriers by the collision mechanisms outlined in chapter 2.

While a photon is absorbed when it energizes an electron to a higher energy band, a photon is created when an electron drops to a lower energy band. The energy of the photon generated is the same as the energy lost by the electron, which is always the energy of the band gap [7].

3.2 Black-Body Radiation

A black-body is defined as an object that is not affected by any outside radiation and emits a spectrum based on its temperature. Since the temperature of an object is proportional to the energy of the electrons within it, the object will emit higher frequency photons with increasing temperature. Thus, by determining the maximum photon flux out of an object at a specific frequency it is possible to measure the temperature of the object [8,9,10, 11,12]. Figure 3.2 illustrates the black-body radiation spectrum of five

different objects at 5 different temperatures [eqn 3.7]. This thesis describes the black body radiation emitted from the discharge plasma of the RIMFIRE gas switch.

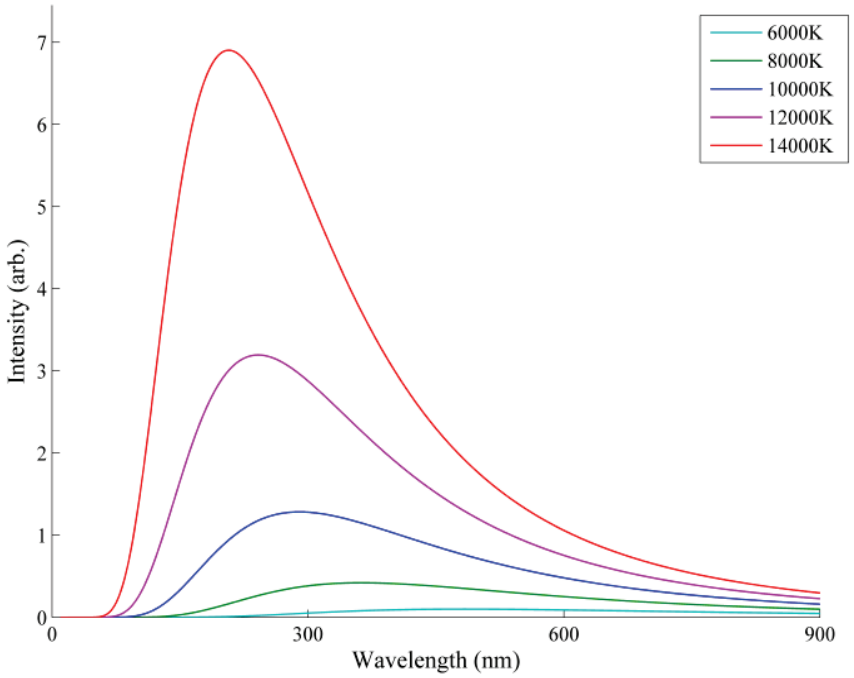

Figure 3.2 The peak of the light spectrum emitted from the object shifts to lower wavelengths of light as the temperature of the object increases [eqn 3.7].

In fully ionized plasma all bound electrons have been removed from their original atoms resulting in a continuous energy spectrum. The plasma arc in the RIMFIRE gas switch is approaching the local thermodynamic equilibrium threshold due to the large current density and optical thickness. To simplify our analysis, it is assumed that the plasma has achieved LTE [9,10,11,12]. Equation 3.5 denotes the time-independent condition of the LTE when the plasma has the same radiation characteristics as a black-body source. Utilizing the Einstein coefficients, the equation takes the form,

$$I_v = \frac{n(q)A(q,p)}{n(p)B(p,q) - n(q)B(q,p)}, \qquad [3.5]$$

where $A(q,p)$ represents the excitation of the upper-level ions by the absorption of photons, $B(p,q)$ and $B(q,p)$ represent de-excitation by spontaneous transition and by induced emission, respectively[8,11]. The intensity, I_v, is in units of [Wm^{-2} sr^{-1} s] and denotes the spectral intensity of the radiation field at the transition frequency $v = 2.8kT/h$. This frequency dependant spectral intensity is related to the plasma temperature by equation 3.6.

$$I_v dv \equiv B_\lambda d\lambda \qquad [3.6]$$

Equation 3.6 can be expanded to Planck's law of equation 3.7 to produce the black-body spectra found in Fig 3.2,

$$I(v,T) = \frac{2hv^3}{c^2} \cdot \frac{1}{e^{\frac{hv}{kT}} - 1} \qquad [3.7]$$

where ***h*** is plank's constant = 6.626×10^{-34}[$J \cdot K^{-1}$], ***k*** is the Boltzmann constant = 1.306×10^{-23}[J·s], ***c*** is the speed of light in a vacuum, and ***v*** is the frequency of electromagnetic radiation [15].

Equation 3.6 is called Planck's distribution or the black-body radiation. Black-body radiation has a maximum photon flux at a certain frequency, depending on the temperature.

$$\lambda_{max} = \frac{2.9 \times 10^{-3}}{T} \text{[m]} \qquad [3.8]$$

$$J^* = \sigma T^4 \text{ [MW m}^{-2}\text{]} \quad [3.9]$$

Equation 3.8 converts the units from temperature in degrees Kelvin to wavelengths in meters. The equation is derived from equation 3.7. Equation 3.9 is called the Stefan-Boltzmann law and it relates the temperature of the plasma in Kelvin to an energy output in MW m^{-2} [16].

3.3 Local Thermodynamic Equilibrium (LTE) and Optical Thickness.

In most laboratory plasmas it is almost impossible to achieve LTE because of low current densities. Low current densities are analogous to low electron densities. In plasmas with low electron densities the radiative rates are larger than the collisional rates. The LTE can only be achieved in high density plasmas where the collisional rates are at least an order of magnitude greater than radiative rates [15]. The plasma in the RIMFIRE gas switch has not achieved absolute LTE, but it is believed to be very close to a black-body spectrum as described in chapter 6 [9].

Plasma that covers a large spatial volume and has high electron density is considered optically thick plasma [8]. In the center of the plasma, photons emit outwards forcing the surrounding plasma to absorb and emit photons. This results in a distribution of photon and electron energies and high collisional rates. The optically thick plasma the more collisions photons must endure before finally being able to radiate out into the surrounding medium. The emitted photons have a black-body distribution because the

electrons have approached LTE and have high rates of collision. The intensity of this photon distribution peaks at a value that corresponds to the temperature as seen in figure 3.2 and equation 3.6. Additional theory on LTE and optical thickness can be found in appendix A [8].

3.4 Generated Charge on the Surface of an Insulator due to UV Flux

The Lambert-Beer law was developed to relate the absorption of photon flux (light) to the properties of the material through which the light is traveling [15]. The law states that there is a logarithmic dependence between the transmission of light **T** through a substance, the absorption coefficient **α**, and the distance the light travels through it **l**. In a gas this relationship is

$$T = \frac{I}{I_0} = e^{-\alpha l} \qquad [3.10]$$

Using the constants relating to pressurized SF_6 gas it can be calculated that SF_6 will easily transmit light down to a wavelength of 160-nm [16]. This indicates that UV flux from the discharge above 160-nm is causing charge formation on the insulator surface due to the photoionization effect described above. Figure 3.3 illustrates the transmission characteristics of pressurized SF_6 gas.

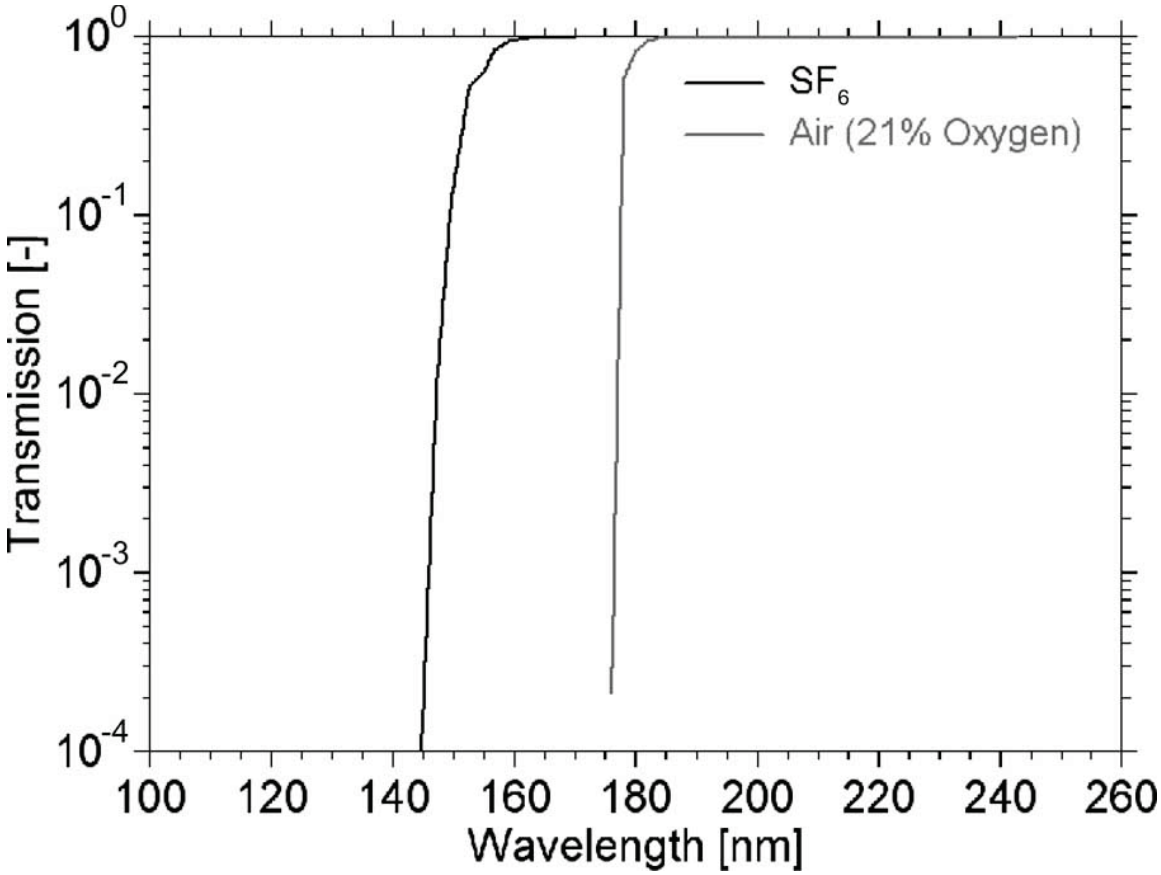

Figure 3.3 This graph shows that SF_6 gas transmits at lower wavelengths than air. SF_6 gas will easily transmit UV light down to 160-nm. This graph was obtained from [10]

Photons incident on the surface of the insulator interact with electrons bound on the insulator surface. The photon loses it energy to the electron forming macroscopic charge gradients along the insulator surface. These gradients may eventually lead to flashover. Previous studies have experimentally documented the impact of photoionization on the surface flashover [2,3,4,17].

The arrival of UV on the insulator surface causes a charge build-up on that surface. Mathematically we can express this surface charging as,

$$\frac{dQ}{dt} = \alpha I(t) - \frac{Q(t)}{\beta}$$

Where *Q (t)* is the charge on the insulator, *I (t)* is the intensity of the UV beam in photons/sec. Thus, *αI(t)* is the rate that the UV produces photoelectrons. As the photoelectrons are swept away from the insulator by the electric field, the surface will develop an increasing positive charge [3].

The absorption and transmission characteristics of PMMA are shown in figure 3.4. This data was obtained from three different samples of PMMA material. The transmission data is the same for all three samples.

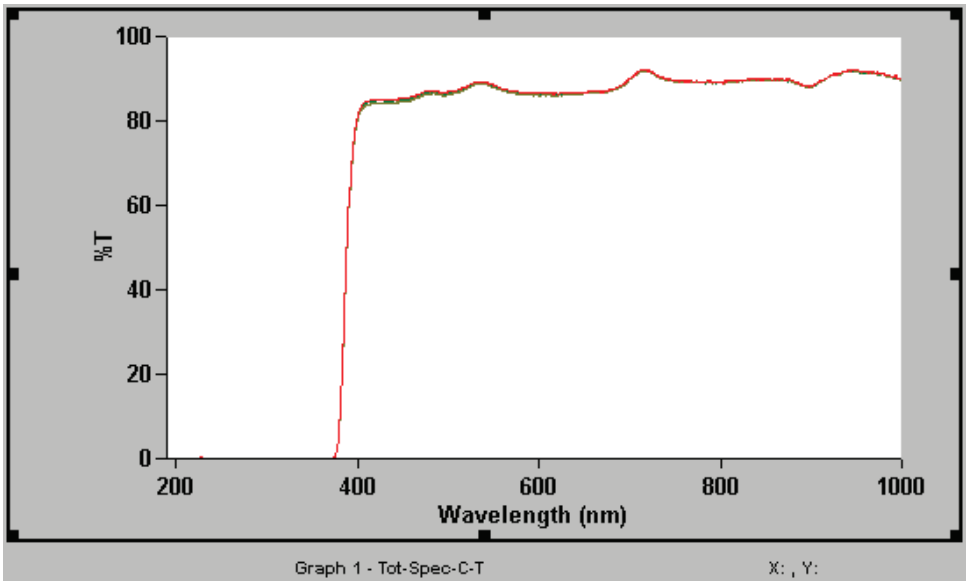

Figure 3.4 Transmittance of light through PMMA from 200 to 1000-nm determined by a Varian Cary50 Spectrophotometer.

The results of the spectrophotometer suggest that the PMMA absorbs all light from 200 to 390-nm. Since the SF_6 gas transmits down to 160-nm, the photon energy from 200 to 390-nm is being absorbed by the PMMA possibly leading to surface charging due to the

creation of free carriers. More transmission and absorption graphs of PMMA can be found in appendix B.

Through spectrographic analysis we have determined that the maximum photon flux incident on the insulator surface has a wavelength of 305-nm. This wavelength of light is absorbed by the PMMA possibly leading to charge accumulation on its surface.

References for Chapter 3

[23] R.F. Pierret, *Advanced Semiconductor Fundamentals*, Pearson Education, New Jersey, 2003.

[24] J.T. Krile, A. Neuber, H. Krompholz, "Effects of UV Illumination on Surface Flashover Under Pulsed Unipolar Excitation", IEEE Conf. Plasma Sci., 2007.

[25] J. Javedani, T. Houck, D. Lahowe, G. Vogtlin, D. Goerz, "Insulator Surface Flashover due to UV Illumination", IEEE. Conf. Pulsed Power, 2009.

[26] V. Svorcik, O. Lyutakov, and I. Huttel, "Thickness Dependence of Refractive Index and Optical Gap of PMMA Layers Prepared Under Electric Field", Journal of Mat. Sci.: Mater Electron, 2008.

[27] T. Yamashita, S. Shichijyo, T. Takemura and K. Matsushige, "Effect of Radiation and Impurities on Microscopic Deformation Process in PMMA", Japanese Journal of App. Physics, 1987.

[28] T. S. Sudarshan, R. A. Dougal, "Mechanisms of Surface Flashover Along Solid Dielectrics in Compressed Gasses: A Review", IEEE Trans. Elec. Insul. Vol. EI-21. No. 5 1986.

[29] R. Morrow and T. Blackburn, "The Role of Photoionization in Streamer Discharge Formation in Voids", IEEE Trans. on Plasma Sci., 1999.

[30] H. R. Griem, *Principles of Plasma Spectroscopy*, Cambridge Univ. Press, UK, 1997.

[31] M. Margoshes, "Excitation and Ionization in Arc and Spark Spectrographic Sources", National Bureau of Standards, Washington, D.C. 20234. 1967.

[32] J.J. Lowke and M. Tanaka, “LTE-diffusion Approximation for Arc Calaculations”, J. Phys. D: Appl. Phys. 39. 2006.

[33] C. Zaepffel, D. Hong, and J. Bauchire, “Experimental Study of an Electrical Discharge Used in Reactive Media Ignition”, J. Phys. D: Appl. Phys. 40. 2007.

[34] V. Bakshi, B. Barrett, T. Boone, and W.C.Nunnally, "Spectroscopic Diagnostics of Railgun Armatures", IEEE Transactions on Magnetics, January, 1993.

[35] T. Nimalasuriya, A. Flikweert, W. Harskamp, “Investigation of Local Thermodynamic Equilibrium in HID Lamps”, ICOPS, 2008.

[36] J.T. Krile, R. Vela, A. Neuber, H. Krompholz, “Spectral Analysis of Pulsed Volume Breakdown in SF_6 at High Pressures”, IEEE Tran. Plasma Sci, vol. 53, 2007.

[37] T. Fujimoto, "Plasma Spectroscopy", Oxford Science Publications, 2007.

[38] A. Sedghinasab, D. Keefer, and H. Crowder, "In-bore Spectral Measurements in a Plasma-Armature Railgun", IEEE Transactions on Plasma Science, June, 1989.

[39] K.P. Morales, J.T. Krile, A. Neuber, H. Krompholz, “Pulsed Dielectric Surface Flashover in Atmospheric Conditions”, IEEE Trans. Diel. Elec. Insu. vol. 13, no. 4, 2006.

Chapter 4 MU Terawatt Test Stand (MUTTS)

The test stand MUTTS is an energy storage system designed to produce a very high-power electromagnetic pulse for various experiments and was originally fabricated by Sandia National Labs [1]. The MUTTS system was part of Sandia National Labs Proto II accelerator and was delivered to MU in 2003. Primarily, MUTTS was used to test a multi-channel laser triggered gas switch. This switch, called RIMFIRE, is utilized in Sandia National Labs Z-Machine to conduct power from the energy store to the water transmission lines [2]. The RIMFIRE switch incorporates a laser triggered gap for timing and a cascade section to limit the switch inductance and electrode erosion. The cascade section was removed and all spectroscopic data was obtained from the trigger section of the switch. MUTTS was disassembled and rebuilt in 2007 with the name TIGER [3]. A block diagram of the MUTTS system is illustrated in figure 4.1.

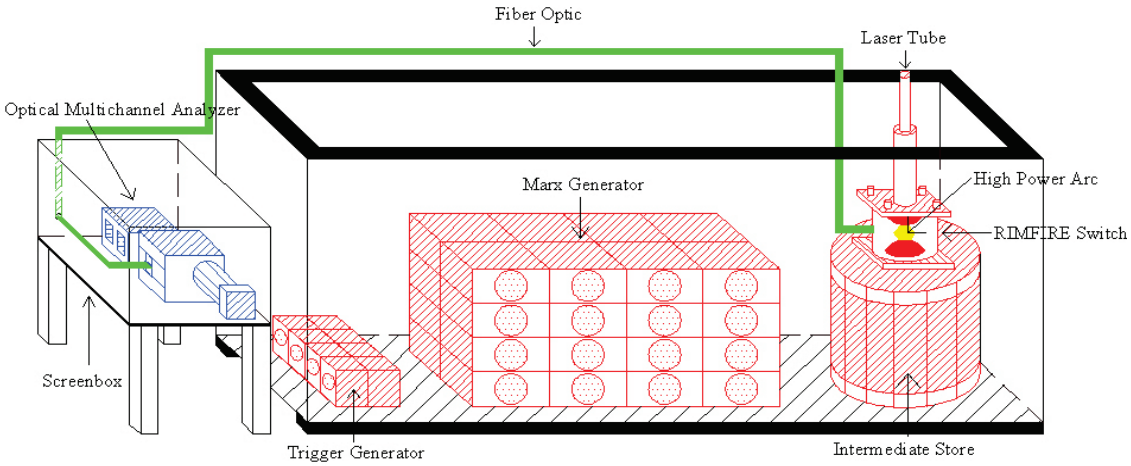

Figure 4.1 This block diagram shows the MUTTS configuration during spectrographic data collection. The Marx trigger generator (MTG) triggers the first row of the Marx generator spark gaps causing Marx erection.

4.1 MUTTS Energy Store

The energy system stores 10-kJ of energy at a 32-kV charge voltage and over 100-kJ at full charge. The trigger gap spacing was set at 4.9-cm and the switch pressure was maintained at 30-psig. The Marx bank is comprised of 32 Aerovox, 100-kV, 700-nF capacitors which are charged by a ±100-kV, 50 mA, Peschel Instruments power supply. This Marx erects through 16 Physics International, T508 spark gaps into 2 parallel, 14-nF, intermediate storage water capacitors. The voltage on the I-Store water capacitors rises with a 1-cosωt waveform across the RIMFIRE gas switch. The 10-90% voltage rise-time is approximately 1-μs. Between 75-100% of peak voltage, the RIMFIRE gas switch self-breaks and discharges the energy into a 4-Ω resistive load. The load consists of eight copper-sulfate water resistors connected in parallel [4]. The basic MUTTS circuit schematic is shown in figure 4.2.

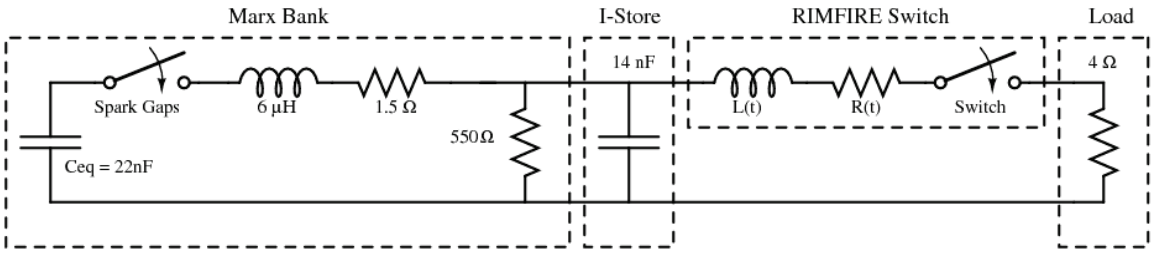

Figure 4.2 This MUTTS circuit is in a CLC discharge configuration which applies a 1.05-MV voltage pulse to the RIMFIRE switch with a 30-kV charge voltage. The switch conducts 130-kA under these conditions [4].

4.2 Electrical Triggering

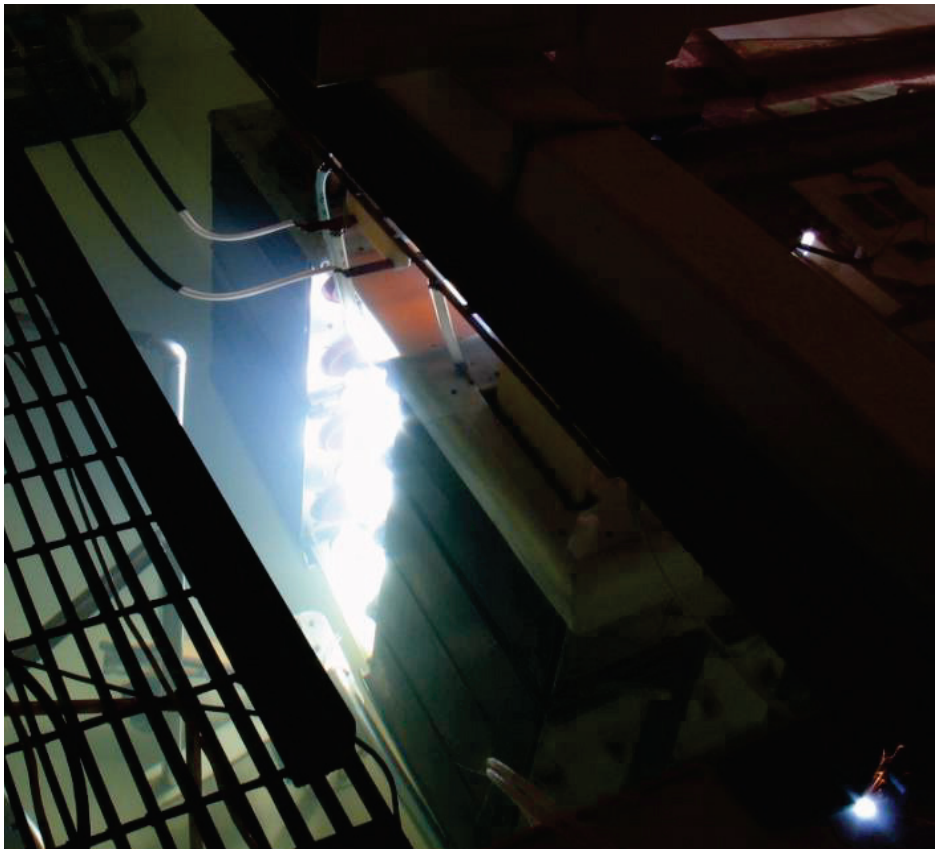

Figure 4.3 This photograph shows the electrical triggering of the first row of the Marx bank spark gaps by the Marx trigger generator (MTG).

The Marx bank of the MUTTS system must be triggered for safe, reliable operation. This trigger system begins with a 10-V trigger pulse from the OMA. This 10-V pulse triggers a Pacific-Atlantic Trade Company PT-003 [5] which subsequently triggers a PT-55 [6]. The PT-55 triggers a Physics International TG-70 [7]. The TG-70 triggers the Marx trigger generator (MTG). The MTG consists of 8, 150-nF, 50-kV Maxwell capacitors which trigger the first row of spark gaps within the main Marx generator. The gas operating curves for each pressurized MUTTS component are shown in figures 4.4 and 4.5.

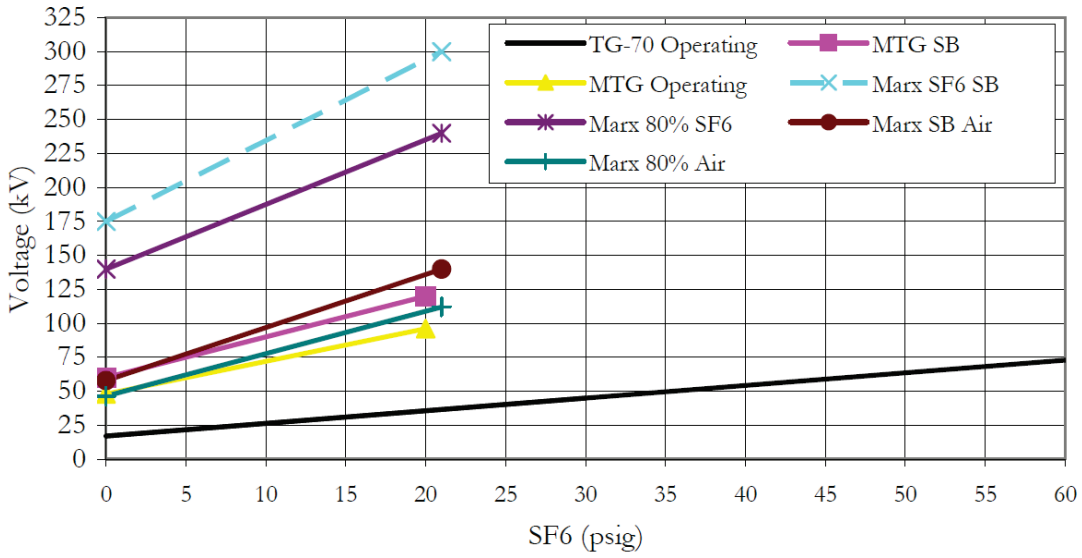

Figure 4.4 This graph, obtained from the dissertation of Dr. Keith LeChien, shows the gas operating curves for the TG-70, MTG, and Marx bank. The electric field breakdown strength increases with increasing gas pressure. [8].

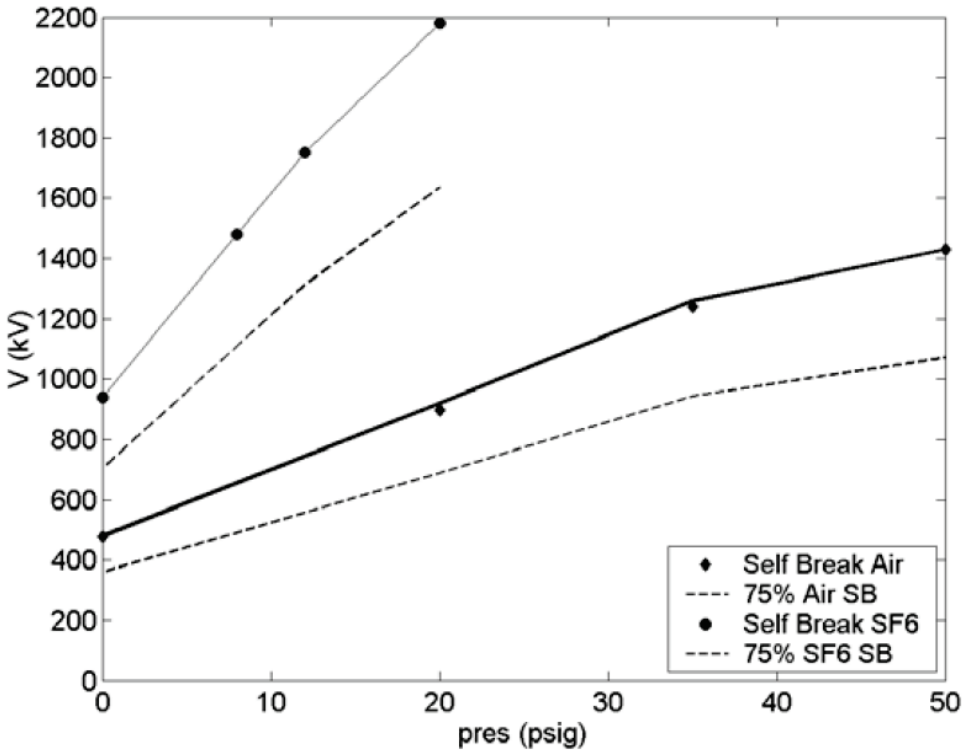

Figure 4.5 This graph, obtained from the dissertation of Dr. Keith LeChien, shows the gas operating curves for the MUTTS RIMFIRE switch. The electric field breakdown strength increases with increasing gas pressure [8].

4.3 Voltage and Current Diagnostics

Several diagnostic systems were implemented to obtain accurate voltage and current measurements from the MUTTS system. The current through the 4-Ω load was measured by 8 T&M Research Model 250-1 current viewing resistors (CVR) [9], placed in series with the load resistors. Each CVR has a 2-ns rise-time with a dissipated energy of 250-J. The Marx generator current was measured with a single CVR. Attenuators were used to reduce the voltages to scope level. Figure 4.6 is a simulated maximum load and Marx voltage from the MUTTS system [1].

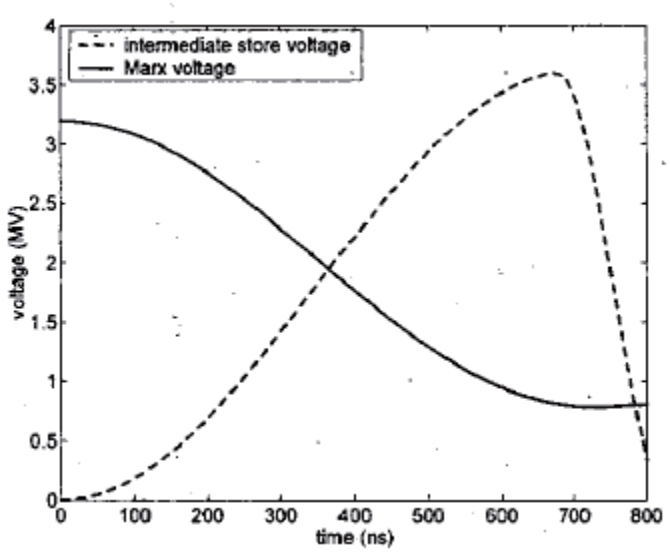

Figure 4.6 This simulation shows that under ideal conditions the MUTTS system is capable of delivering a 3.5-MV pulse to a load in 700-ns [1].

The voltage across the 4-Ω load was measured by a voltage divider and a 52.4-Ω high voltage attenuator. The voltage divider had a ratio of 1220:1 and the high voltage attenuator had a ratio of 17.7:1. These two dividers coupled with a 6-dB attenuator reduced the 1.2-MV pulse to 28-V. The Marx generator voltage was measured with a

voltage divider and a 49.7-Ω high voltage attenuator. The I-Store voltage was measured with a voltage divider and a 48-Ω high voltage attenuator [3]. The voltage and current measurements from a typical discharge are shown in figure 4.7.

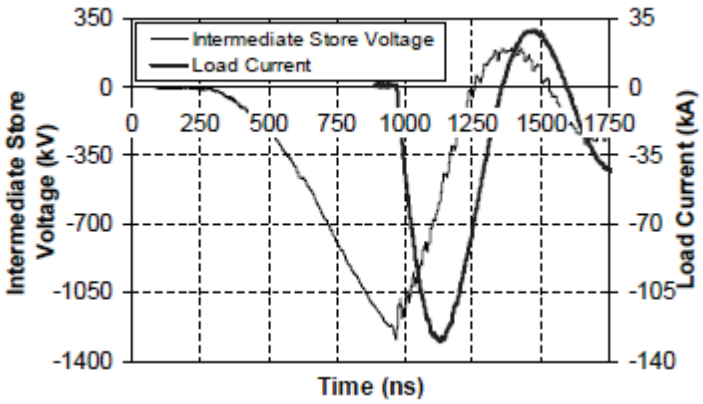

Figure 4.7 This graph shows a typical pulse from MUTTS. The peak voltage and current values are 1.25-MV and 130-KA, respectively [4].

4.4 Optical Diagnostics

The optical diagnostics of the MUTTS system consist of an optical multichannel analyzer (OMA), a fiber optic, a Canon Powershot A75 camera, and two calibration source lamps. The OMA is a spectrograph coupled to an ICCD camera. The fiber optic was brought into the screen box through a 12" copper tube. A photograph of the system confined in its electromagnetically shielded screen box is shown as figure 4.8.

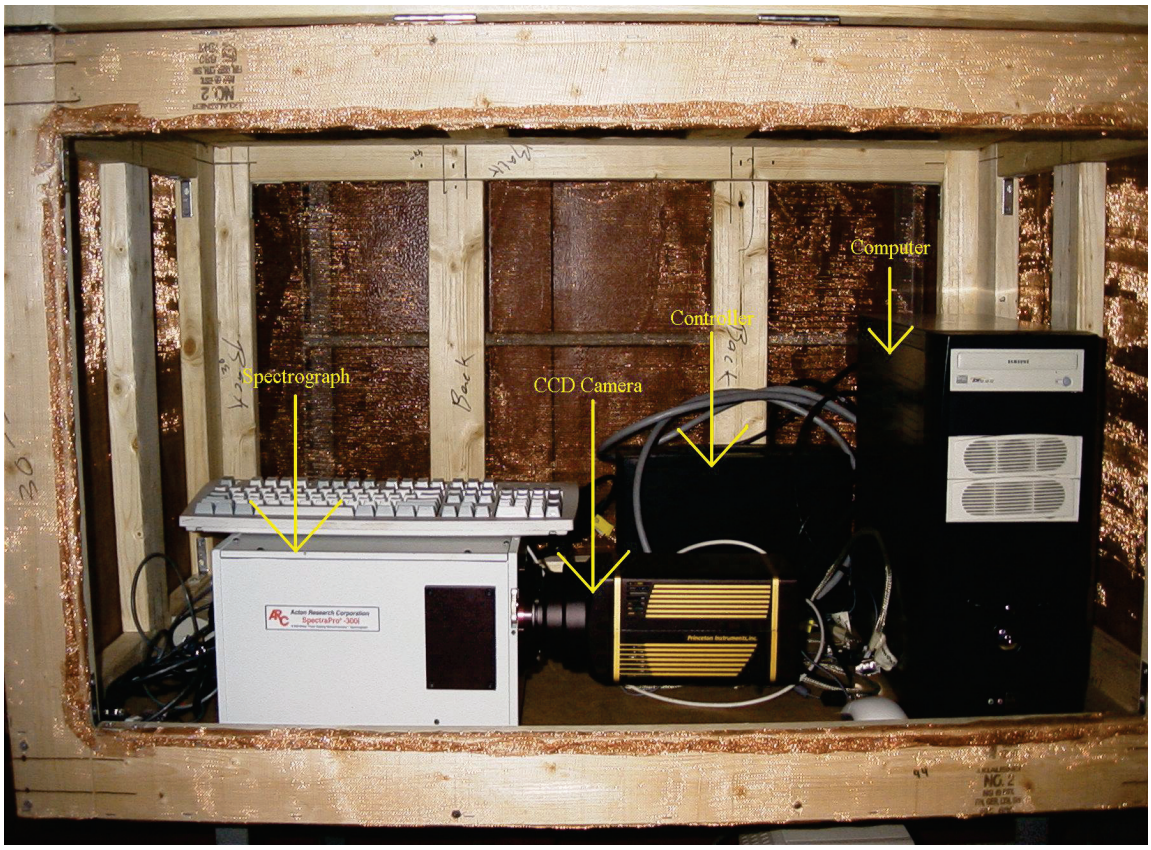

Figure 4.8 This photograph shows the location of the OMA diagnostic inside the shielded screen box. The screen box prevents MUTTS electromagnetic noise from interfering with OMA signal quality.

4.4.1 Optical Multichannel Analyzer Specifications

The OMA consists of an Acton Research Corporation SpectraPro-300i spectrograph [11], a Princeton Instruments ICCD-MAX Intensified CCD camera [12], a ST-133 Controller [13], and a desktop computer equipped with the PCI card for the spectrograph and controller. The following specifications describe the capabilities of each component:

Table 4.1. List of OMA Hardware

Acton Research Corporation SpectraPro-300i	
Focal Length:	300nm
Aperture Ratio:	f/4
Optical Design:	Imaging Czerny-Turner with original polished aspheric mirrors
Optical Paths:	90° standard
Scan Range:	0 to 1400nm mechanical range
Gratings:	300-g/mm, 600-g/mm, 1200-g/mm
Operating Range:	185nm to far infrared
Resolution:	0.1nm at 435.8nm
Dispersion:	2.7nm/mm
Standard Slits:	Micrometer adjustable from 10um to 3mm wide
Coupling:	Adjustable slit SMA connection for fiber optics
Princeton Instruments ICCD-MAX Intensified CCD Camera	
EEV 1024 x 256:	Full frame, 26 x 26 um pixels
Well Capacity:	500 ke typical; with binning 1.2 Me
CCD R. Noise:	< 1.6 cnts rms @ 100kHz ; < 3 cnts rms @ 1 MHz
Gain:	Fixed at 10 e per count up to 255 count
Image Intensifier:	18 mm
Focal Depth:	0.894”
Resolution:	Typically 45 um spot size FWHM
Spectral Range:	Red-blue enhanced, 180-900nm
Max Rep. Rate:	Sustained: 50 kHz ; Burst: 250 kHz (50 pulse burst)
MCP Bracket Pulsing:	Enabled
ST-133 Controller for ICCD-MAX Intensified CCD Camera	
Data Transfer:	1 megapixel per second
Triggering:	PTG Input/Output
Op. Modes:	Continuous; Sequential; Anticipated Trigger
Trig. Modes:	Internal; External
Software:	WinSpec/32

4.4.2 Fiber Optic Specifications

The fiber optic was made of quartz-silica material which allowed complete light transmission between 200 and 800-nm. The fiber diameter is 400-µm to allow for transmission of large amounts of photon flux without attenuation. To allow for adequate distance between the OMA and the RIMFIRE plasma, the fiber was made 16 meters long. Eight meters of Kevlar jacketing were included for added protection. One end of the fiber was polished with 0.3-µm lapping film while the other terminated into an SMA connection. Figure 4.9 shows the typical transmission characteristics of our fiber optic from the manufacturer specifications.

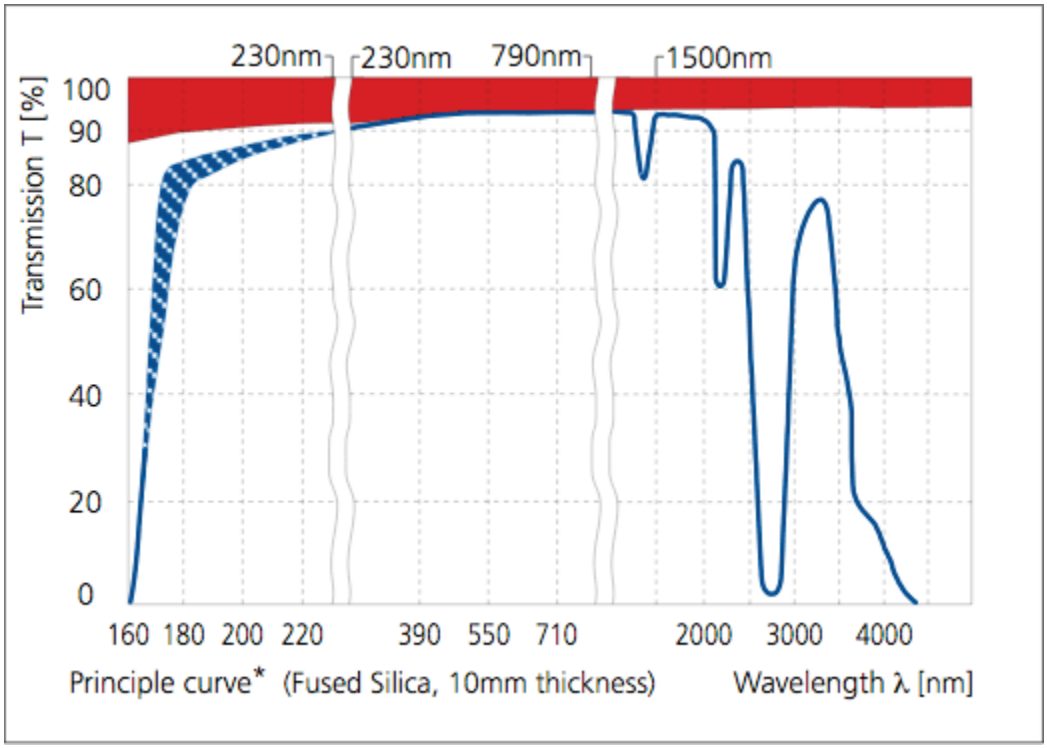

Figure 4.9 Typical transmission characteristics of a fused quartz-silica fiber optic. There is an aproximate transmission profile between 200 and 800-nm. This graph was obtained from the website of Prazisions Glass and Optic [14].

4.4.3 Canon Powershot A75 Camera

A sample photograph taken using the Canon A75 camera is shown in figure 4.10 [15]. The camera was operated in open shutter mode to catch the entire current pulse. A neutral density filter was used to reduce the photon flux on the camera. This photograph helps classify the plasma as optically thick.

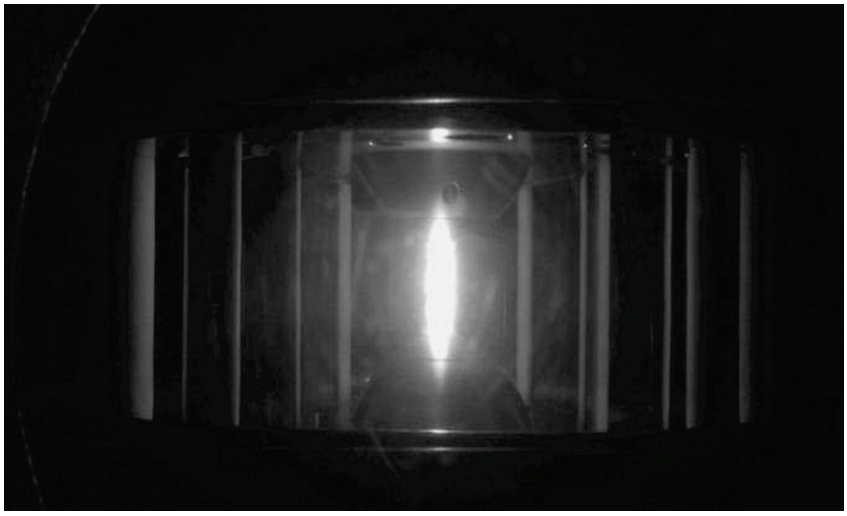

Figure 4.10 Typical breakdown arc of the RIMFIRE gas switch. This light is transmitted through a fiber optic into an OMA for analysis.

4.4.4 Calibration Source Lamps

The spectral data was calibrated by two spectral irradiance lamps: a 30 watt deuterium lamp calibrated to output a spectrum between 200 and 400-nm and a 200 watt QTH lamp calibrated to output a spectrum between of 250 and 2400-nm. Both of the lamps were calibrated to NIST standards EH6924 and F-525, respectively [16]. The lamps were used to calibrate the OMA spectra. This procedure is explained in a later section.

4.5 RIMFIRE Gas Switch

The RIMFIRE gas switch is composed of two physical sections: a trigger section and a cascade section. The purpose of the cascade section is to limit switch inductance and reduce electrode erosion [17]. The cascade section was removed and only the trigger section was tested. Figure 4.11 is a 3D model of the RIMFIRE gas switch with the cascade section included. The trigger gap spacing was set at 4.9-cm and the switch pressure was maintained at 30-psig.

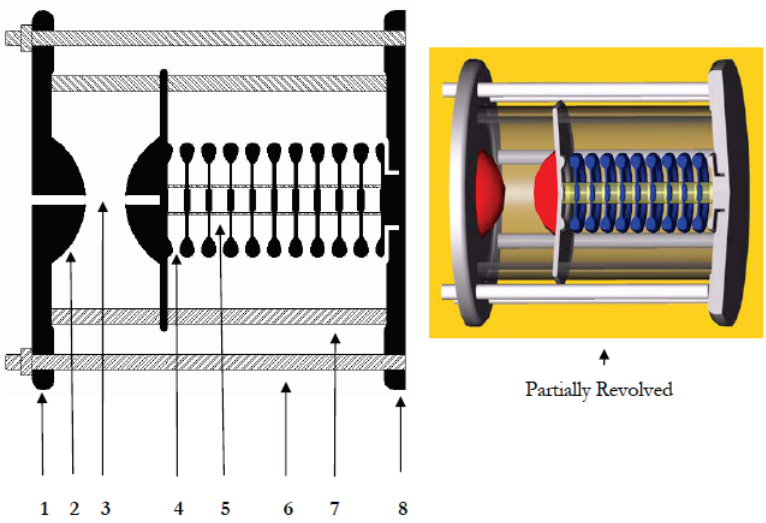

Figure 4.11 The numbers from 1-8 refer to, in order, 1 load end (aluminum), 2 trigger electrode with hole for laser(stainless/Mallory), 3 trigger gap (gas dielectric), 4 cascade gap, ten total (gas dielectric, stainless electrodes), 5 cascade spacer (acrylic), 6 tie rod (nylon), 7 gas envelope (PMMA acrylic), 8 I-Store/high voltage end (aluminum) [18].

The trigger section is composed of the two hemispherical electrodes shown in figure 4.11 and the left side of the switch modeled in figure 4.10. With the cascade section removed, the rated voltage of the switch drops from approximately 4-MV down to 1.5-MV [19]. The fiber optic is located in close proximity to the breakdown plasma through a hole drilled in the PMMA gas envelope, and epoxyed in place.

REFERENCES FOR CHAPTER 4

[1] K. LeChien, J. Gahl, M. Kemp, and R. Curry, "Development of a Terawatt Test Stand at the University of Missouri for Fast, Multichannel Switching Analysis", IEEE Conf. Pulsed Power, 2003.

[2] K. Rosenthal, S.E.; Elizondo, J.M.; Maenchen, J.E.; Struve, K.W.; McDaniel, D.H.; Corley, J.P.; Johnson, D.L.; Oliver, B.V., "Modeling 6 MV Gas Switches for the ZR Accelerator", 14th IEEE Pulsed Power Conference, 2003.

[3] A. Benwell, J. Vangordon, D. Sullivan, B. Hutsel, S. Kovaleski, J. Gahl, "A 2.8-MV, 600-kA Pulsed Power Driver Constructed at the University of Missouri-Columbia", IEEE Conf. Plasma Sci., 2007.

[4] M. Kemp, R. Curry, and S. Kovaleski, "Experimental Study of the Multichanneling Self-Break Section of the Rimfire Switch", IEEE Transactions on Plasma Science, 2006.

[5] Model PT-300-S, Solid State Trigger Generator, Pacific Atlantic Electronics.

[6] Model PT-55-S, Pulser/Trigger Generator, Pacific Atlantic Electroncs.

[7] Model TG-70, Trigger Generator, Physics International.

[8] K. LeChien, "Implementation of the University of Missouri Terawatt Test Stand and the Study of a Large, Multichanneling, Laser Triggered Gas Switch", Dissertation, University of Missouri – Columbia, 2006.

[9] Model 250-1, Current Viewing Resistors, T&M Research Products.

[10] M. Kemp, "Simulation and Experimental Study of the Multichanneling RIMFIRE Gas Switch", Thesis, University of Missouri – Columbia, 2005.

[11] SpectraPro 300i, Spectrograph, Acton Research Corporation. Manual.

[12] ICCD-MAX, Intensified CCD Camera, Princeton Instruments. Manual.

[13] ST-133, Spectrograph Controller, Princeton Instruments. Manual.

[14] Prazisions Glass and Optic: http://www.pgoonline.com.

[15] PowerShot A75, Camera, Canon, Manual.

[16] Calibration Lamps, Newport-Oriel, Manual.

[17] K. LeChien, J. Gaul, and K. Struve, "Electrical Effects of Multichanneling in the 2.5 MV Rimfire Gas Switch using a Laser Trigger", IEEE Pulsed Power Conference, 2005.

[18] A. Benwell, S. Kovaleski, J. Gaul, M. Kemp, and K. LeChien, "Insulator Breakdown Tests Preceding a Study of Magnetic Flashover Inhibition", IEEE Pulsed Power Conference, 2005.

[19] S. Kovaleski, J. Gaul, D. Swarts, C. Yeckel, A. Benwell, and R. Curry, "Investigation of Causes Leading to Dielectric Flashover in a Laser Triggered Gas Switch", ICOPS, 2006.

Chapter 5 Experimental Design

The RIMFIRE gas switch was modified to allow spectrographic analysis of the breakdown plasma. The cascade section was removed and all spectra were obtained from the RIMFIRE's trigger section. The fiber was brought into close proximity to the plasma through holes drilled in the plastic insulator. The fibers glued into the insulator are pictured in figure 5.1. The holes in the insulator wall for the fiber optic were drilled with a 0.4318-mm diameter bit. The epoxy used to bond the fiber to the insulator was AngstromBond® AB 9113SC [1].

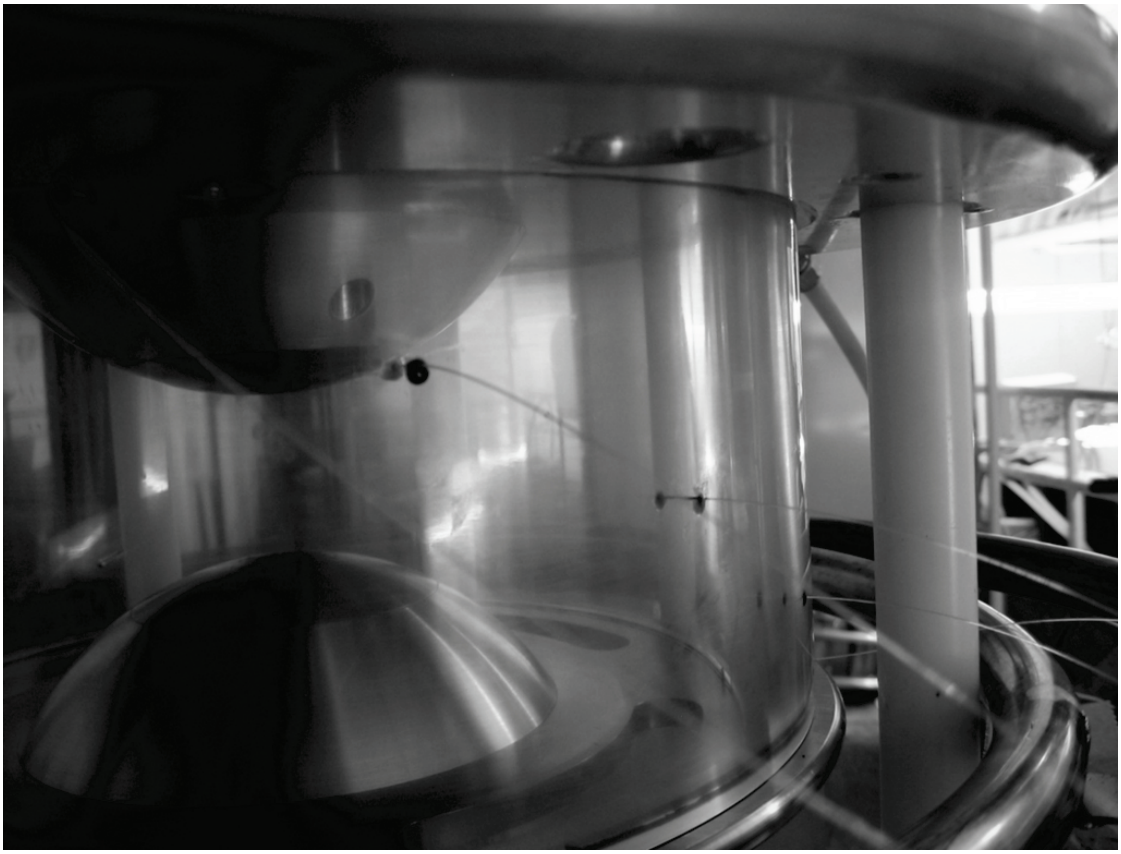

Figure 5.1 The fibers are placed through holes in the insulator and fixed with an epoxy formulated to bond glass to plastic. The hemispherical electrodes can be clearly seen in this photograph.

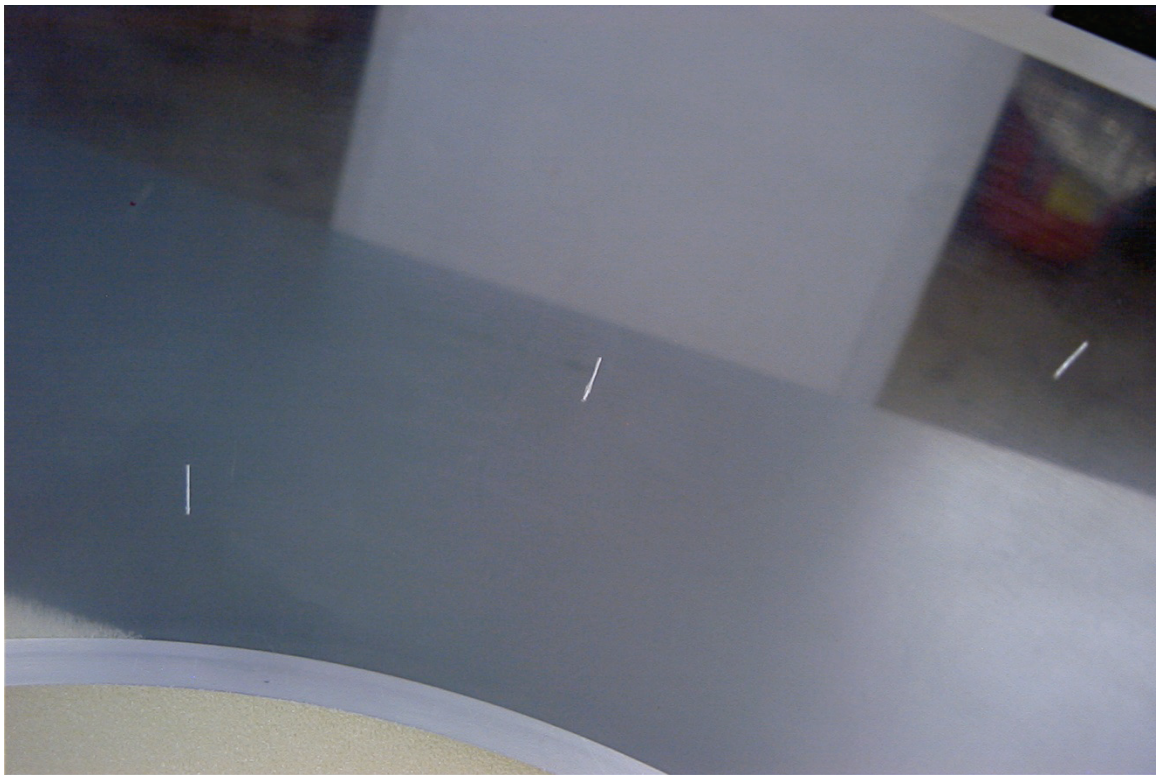

Figure 5.2 Photograph of holes drilled in the PMMA insulator.

5.1 Transmittance and Absorbance of PMMA

The motivation for testing the transmission and absorption of the PMMA is that the UV flux generated by the RIMFIRE breakdown plasma was thought to be depositing charge on the surface of the PMMA insulator leading to flashover. The tests indicate that UV flux below 380-nm was completely absorbed by the PMMA possibly leading to charge accumulation on the plastic's surface [2,3,4]. The PMMA polymer is found to have a gradual transmission cutoff between 380 and 400-nm.

The PMMA samples tested were 0.5 centimeters in depth and there were nine samples tested. The samples were tested with a Varian Cary50 Spectrophotometer. A spectrophotometer sweeps a sample with light from varying wavelengths to determine transmission and absorption characteristics. These samples were split into three sets of

three. The first set was wiped clean with a lint-free cloth. The second set was cleaned with hexane using a lint free cloth. The third set was cleaned with Windex using a lint free cloth. There were three sets of data taken per set of samples. The entire spectrum (190-1000nm) was scanned across the first sample set (3 pieces) with its three cleaning procedures. The last two sample sets (6 pieces) were scanned at very low speed between (410nm and 370nm) to generate the greatest resolution at the cutoff. Below are the cutoff graphs from the second set of data. All seven cutoff graphs can be found in appendix B.

For the cutoff graphs: A = no cleaning, B = Hexane, and C = Windex, when looking at the graph key. The two variables graphed were %Transmitted (%T) and Absorption (Abs). The last graph pinpoints an anomaly that was found at about 225 nm. There appears to be some transmission at that wavelength.

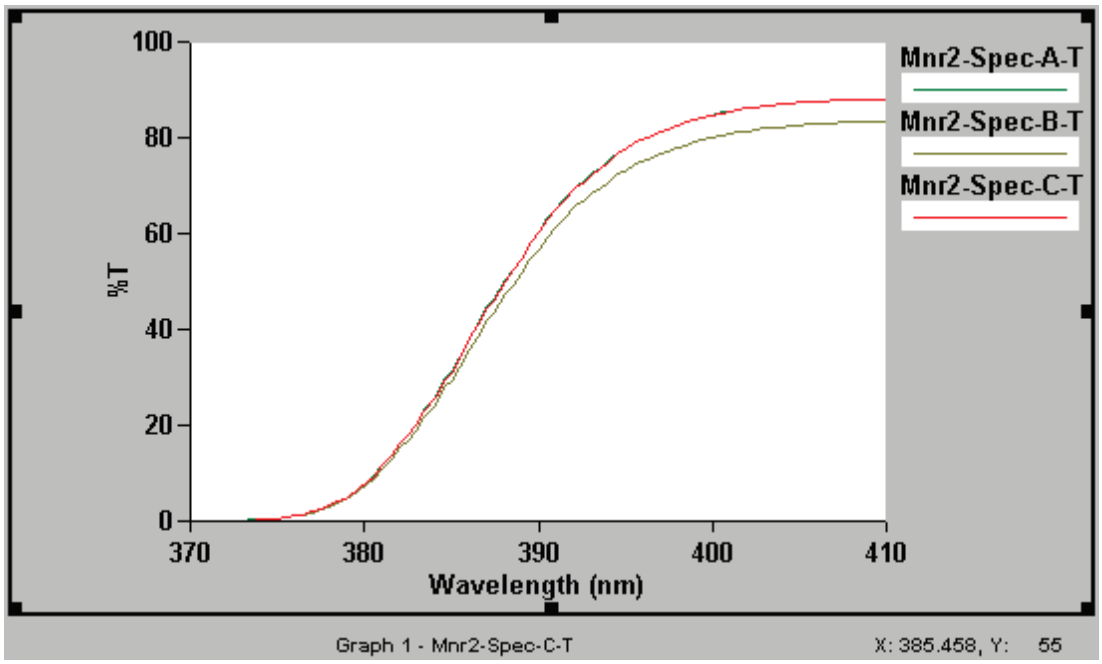

Figure 5.3 This graph shows that the cutoff region of PMMA is between 400 and 380-nm. Between these wavelengths the %Transmitted drops about 80%. It is also apparent that the PMMA cleaned with hexane exhibits lower transmission when nearing cutoff.

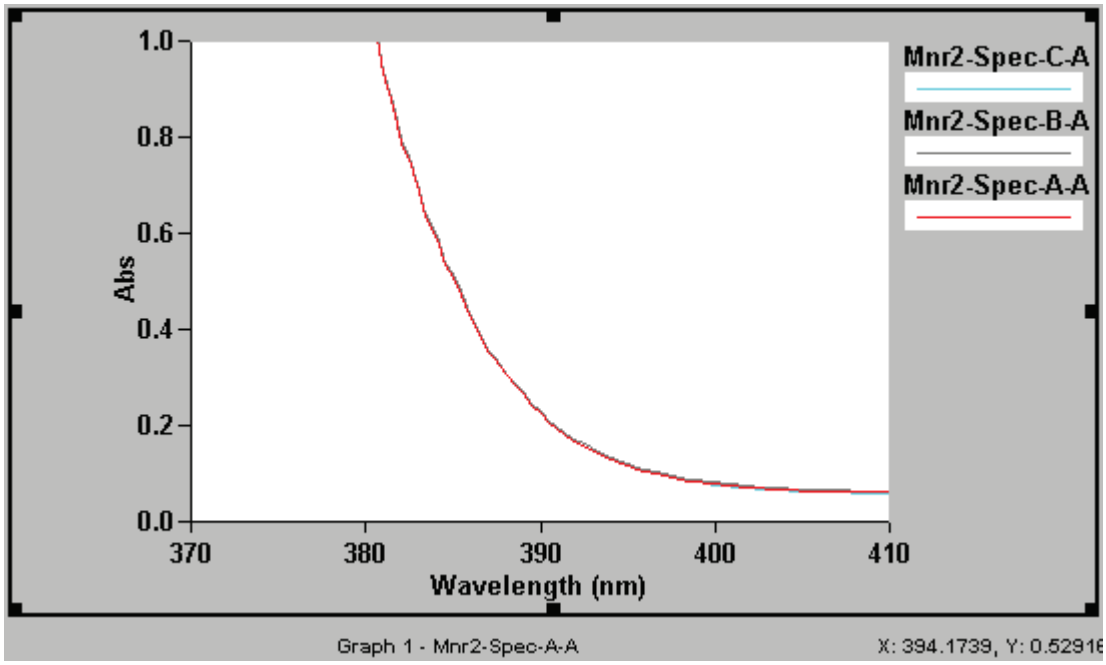

Figure 5.4 This graph shows that the cutoff region is between 400 and 380-nm. Between these wavelengths the amount absorbed increases from about 0.1 to 1.0. There is no apparent increase in absorption due to hexane.

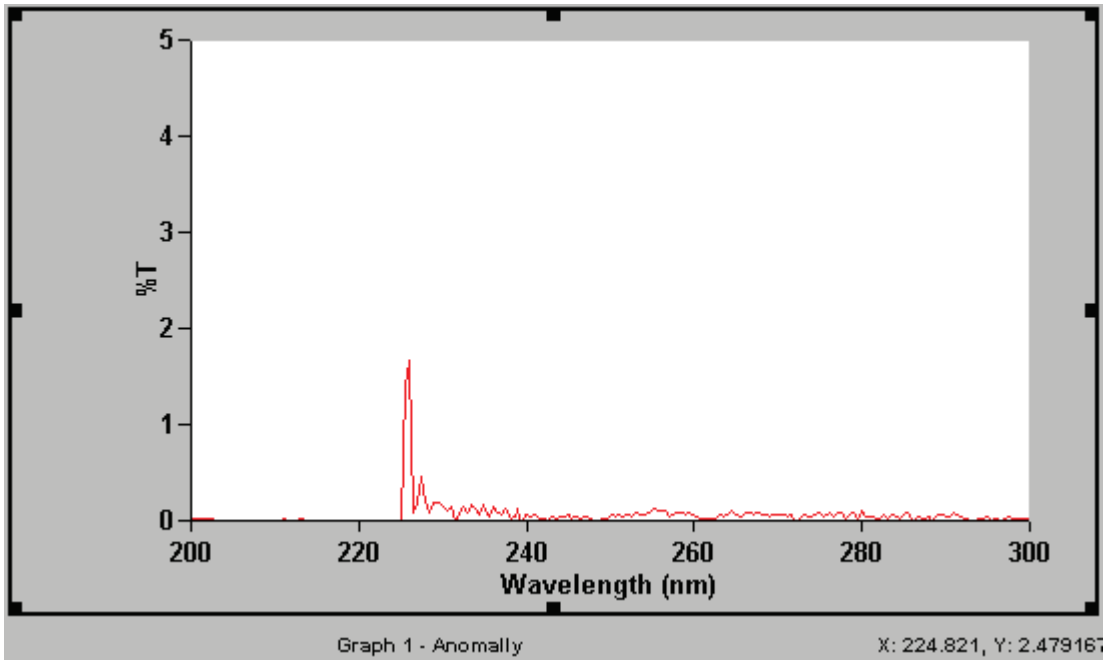

Figure 5.5 This graph shows an anomaly within the PMMA. It appears that at wavelengths of around 225-nm, a 2% transmission occurs. This anomaly was verified with repeated tests with other samples.

5.2 OMA Timing Considerations

Before any testing could be performed a detailed timing diagram for the Marx system was developed. This timing diagram is shown in Fig 5.6. It was shown that, on average, the switch began to conduct current approximately 300-µs after the programmed ICCD controller delay. The ICCD camera was optically triggered to gate 294-µs after the firing procedure was initiated to ensure that the spectrum included the entire current pulse. It also ensured that the light transmitted through the fiber was intense enough for accurate spectrographic measurement.

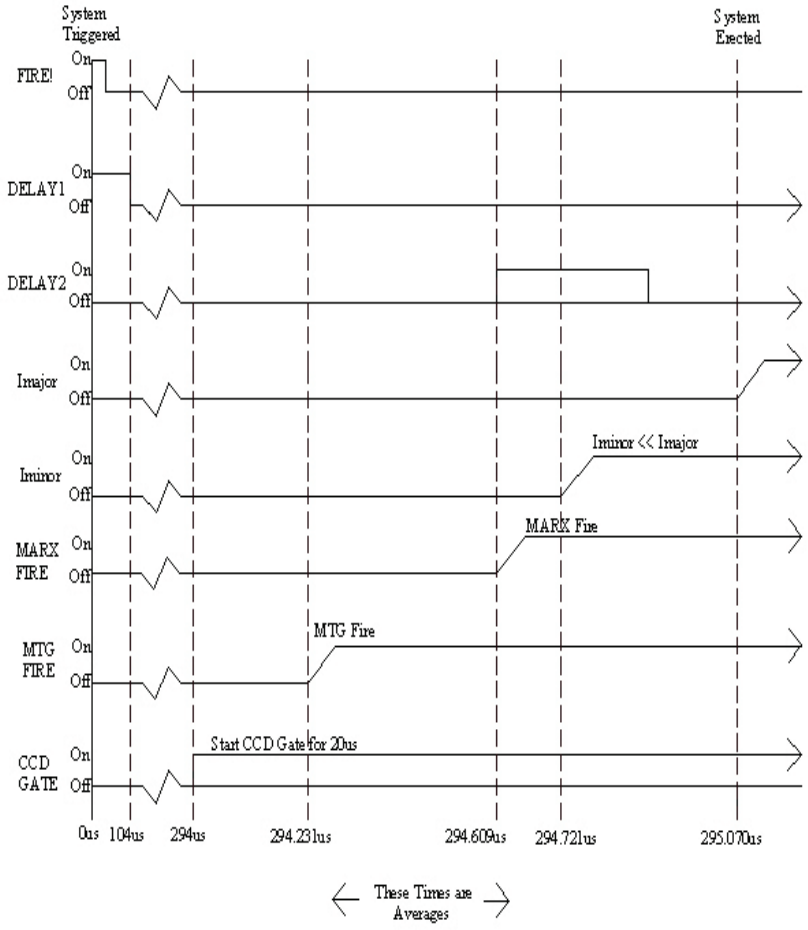

Figure 5.6 This timing diagram was developed from voltage signals of the various electrical components. This diagram was developed from the average of approximately 30 discharges. The OMA controller set the delay at 294-µs and then triggered the discharge. I major is the primary discharge arc.

Correct timing is vital to spectrographic data collection. The CCD was set by the controller to gate for 20-µs. This ensures that light from the entire current pulse was transmitted through the fiber optic to the OMA. The MTG fired 230-ns after the CCD controller trigger signal. The Marx fired after 609-ns and the RIMFIRE gas switch fired after 1070-ns.

5.3 OMA Settings

The spectrometer slit width was set at 26-µm for every test. The center wavelength, number of tests, intensifier setting, CCD gate length, and grating number for the tests taken are listed in Tab 1. A total of 40 tests were performed. Two spectra at 289-nm were found to be corrupted.

Table 5.1 Spectrograph/CCD settings for 38 tests performed.

Center Wavelength	Tests	Gain	Gate	Grating
210 nm	5	255	20 µs	1200g/mm
249 nm	5	255	20 µs	1200g/mm
289 nm	3	100	20 µs	1200g/mm
300 nm	5	50	20 µs	600g/mm
387 nm	5	50	20 µs	600g/mm
438 nm	5	0	20 µs	300g/mm
474 nm	5	50	20 µs	600g/mm
617 nm	5	0	20 µs	300g/mm

Tests were performed with a Marx bank charge of 32-kV. Simulations show that this charge voltage translates to a switch voltage and current of 1.2-MV and 150-kA, respectively. The pressure of the SF6 gas in the switch was held at 30-psig. The switch was purged of its SF_6 gas and repressurized after every 5 shots to eliminate breakdown byproducts from influencing spectrographic results. The trigger gap spacing was set at 4.9-cm and the switch pressure was maintained at 30-psig for every shot.

REFERENCES FOR CHAPTER 5

[20] AB 9113SC, Fiber Epoxy, AngstromBond, Manual.

[21] J.T. Krile, A. Neuber, H. Krompholz, "Effects of UV Illumination on Surface Flashover Under Pulsed Unipolar Excitation", IEEE Conf. Plasma Sci., 2007.

[22] J. Javedani, T. Houck, D. Lahowe, G. Vogtlin, D. Goerz, "Insulator Surface Flashover due to UV Illumination", IEEE. Conf. Pulsed Power, 2009.

[23] D. Korowicz, P. Kelly, K. Mongey, and G. Crean, "Surface Charge Analysis Characterization of Ultra-Violet Induced Damage in Silicon Nitride Dielectrics", Science Direct Applied Surface Science, 2000.

[24] Cary50, Spectrophotometer, Varian, Manual.

[25] A. Kumada, S. Okabe, "Resolution and Signal Processing Technique of Surface Charge Density Measurement [on PMMA] with Electrostatic Probe", IEEE Trans on Diel. Insl. Vol. 11. No. 1, 2004.

Chapter 6 Spectra Calibration and Results

The raw breakdown plasma spectra transmitted through the fiber optic and measured by the OMA was calibrated to obtain the correct spectra data. Spectral inefficiencies in both the fiber optic and OMA can lead to erroneous data, so calibration lamps must be used to correct the raw spectra. The calibration lamps output a broad spectrum that is also transmitted through the fiber and OMA. Since the output of the lamps is known, discrepancies between the actual lamp output and the measured output can be resolved. The measured discrepancies can then be applied to the raw spectra of the switch plasma to produce the corrected spectra.

The spectrograph utilized was an Acton Research Corporation SpectraPro-300i. The spectrograph consists of three diffraction gratings which correspond to three different resolutions: a 300-g/mm grating blazed at 500-nm, a 600-g/mm grating blazed at 500-nm, and a 1200-g/mm grating blazed at 300-nm. A larger number of grooves/mm indicates a higher resolution and a shorter spectral range. The blaze determines where the grating spectral intensity is the most efficient. Since the spectrograph has varying efficiencies at different wavelengths, calibration was necessary to obtain accurate spectral data.

Preliminary wavelength calibrations were performed in WINSpec [1] software by a mercury-argon lamp. This calibration ensures that the software, spectrograph, and CCD camera are spectrally resolved in terms of the wavelength. The CCD camera is an Intensified Princeton Instruments ICCD-MAX. This camera incorporates a 1024x256

pixel chip with each pixel being 26x26-μm. The camera is used in gate-mode with a trigger signal being provided by the programmable timing generator (PTG) of a ST-133 controller. The camera is equipped with a Gen-III intensifier.

6.1 Calibration Procedure

The spectral data was calibrated by two spectral irradiance lamps: a 30 watt deuterium lamp calibrated to an output spectrum of 200 and 400-nm and a 200 watt QTH lamp calibrated to an output spectrum of 250 and 2400-nm. Both of the lamps were recently calibrated to NIST standards EH6924 and F-525, respectively. The CCD was removed from the spectrometer and a flat-field correction was obtained with a fluorescent lamp. The flat-field correction was necessary to correct pixel quantum efficiencies. As the CCD degrades over time and the pixel outputs begin to differ slightly from each other. A flat-field correction fixes these discrepancies.

The data from each of the five breakdown spectra at each center wavelength were then averaged together. This averaging reduced error generated by differing intensities between shots. At the 289-nm center wavelength only three spectra were averaged since two of the spectra data files were corrupted.

For example, the pixel intensities per wavelength of all 5 breakdown spectra at the center wavelength of 300 nm were averaged, and then 301-nm, and then 302-nm, and so on. Equation 6.1 explains this calibration procedure clearly. An immovable circular aperture on the CCD limited the valid 0-1024 pixel range to 185-815 and the rest of the pixels

were removed. The data recorded by the OMA was an array of 631 x 256 pixels. Each pixel stores the photon count (intensity) that was collected at the pixel. The intensity values of the vertical pixel columns were then summed for each wavelength. This summing procedure created a 631 x 1 array with one intensity value per wavelength. The calibration procedure is demonstrated by equation 1 where S1 indicates the first breakdown; S2 indicates the second breakdown, etc.

$$\mathrm{Spec}_{300\mathrm{nm}} = \frac{(\mathrm{S1}_{300}+\mathrm{S2}_{300}+\mathrm{S3}_{300}+\mathrm{S4}_{300}+\mathrm{S}_{300})/5}{\mathrm{Flatfield\ x\ Calibration}_{300}\ \mathrm{x\ Lamp\ Output}_{300}} \qquad [6.1]$$

To calibrate these spectra, the spectral irradiance lamps were transmitted through the fiber into the OMA at each of the center wavelengths. The gain on the intensifier was the same for both the calibrated and breakdown spectra. These calibration spectra were then submitted to the same binning parameters as the breakdown spectra, with each wavelength corresponding to one intensity value. The breakdown spectra were then divided by these calibration spectra. The flat-field correction was then applied to these spectra to account for CCD pixel variance. The last correction involves the output of the lamps themselves. Since the lamps have different outputs at different wavelengths, the spectra must be divided by the curve equation correction provided in the lamps' calibration file. Figures 6.1 and 6.2 show the broad output spectra of the QTH lamp and the deuterium lamp, respectively. Appendix C includes the equations that produce the spectra in figures 6.1 and 6.2.

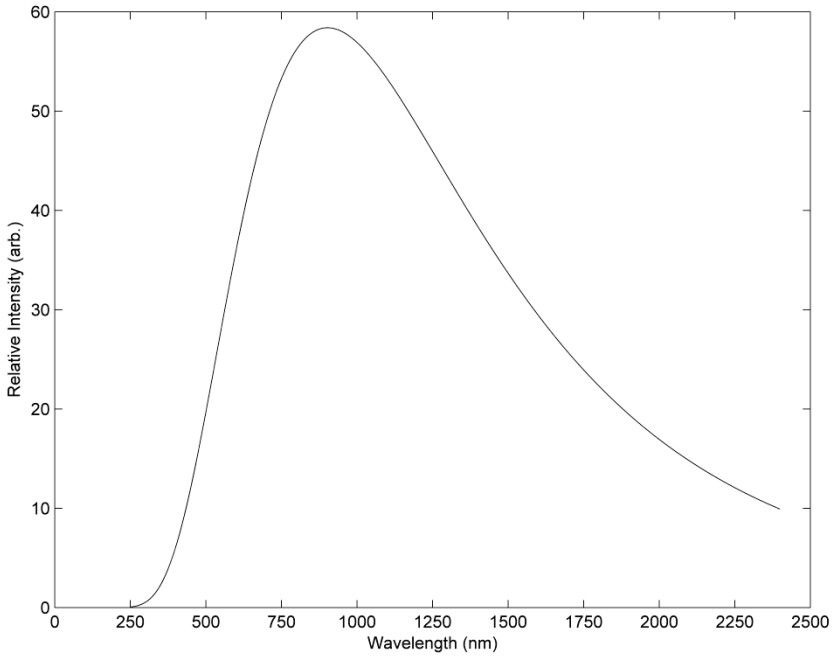

Figure 6.1 QTH lamp calibration source output spectrum. This known spectrum is used to calibrate the breakdown plasma spectra.

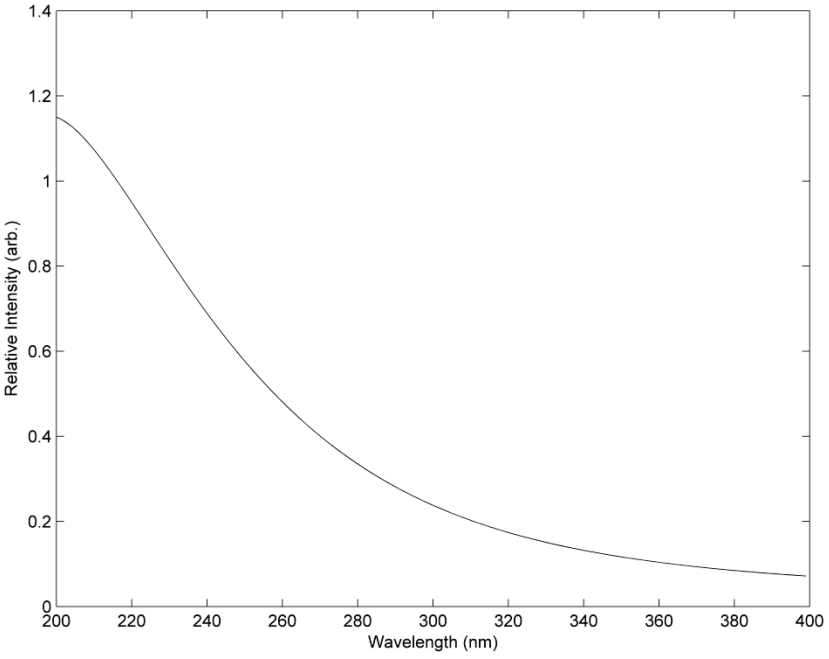

Figure 6.2 Deuterium lamp calibration source output spectrum. This known spectrum is used to calibrate the breakdown plasma spectra.

6.2 Raw Spectra

The raw (pre-calibrated) spectra are reported in this section. Each raw file presented was binned and averaged, but no calibration divisions were applied. Four spectra are presented corresponding to the four different CCD intensifier gains utilized. These gains are listed in table 4.1. Figure 6.3 is the spectra obtained with the gain at 255 at center wavelengths of 210 and 249-nm. Both the fiber and the CCD have different spectral efficiencies, so these spectra should not be considered an accurate spectral model of the breakdown plasma. The figures are included to show that the spectra align relatively well.

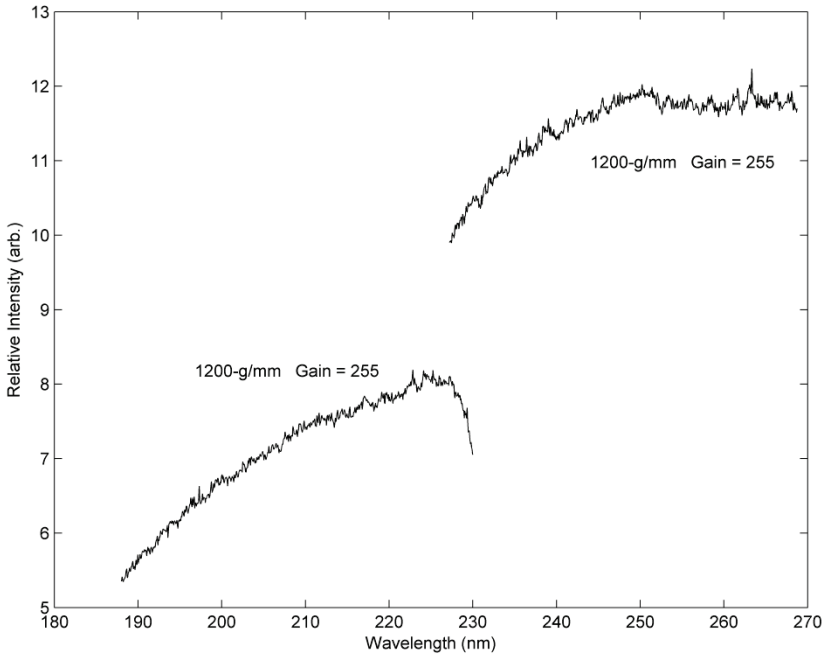

Figure 6.3 These two spectra were obtained using the 1200-g/mm grating, which is blazed at 300-nm, and a CCD intensifier gain of 255. Each spectrum is the average of five different breakdowns.

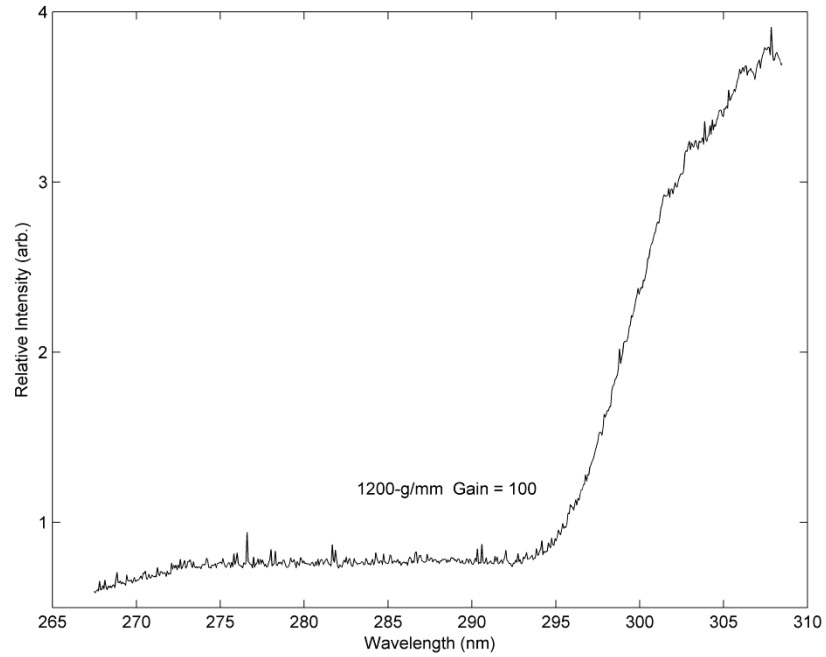

Figure 6.4 This spectrum was obtained using the 1200-g/mm grating, which is blazed at 300-nm, and a CCD intensifier gain of 100. The spectrum is the average of three different breakdowns.

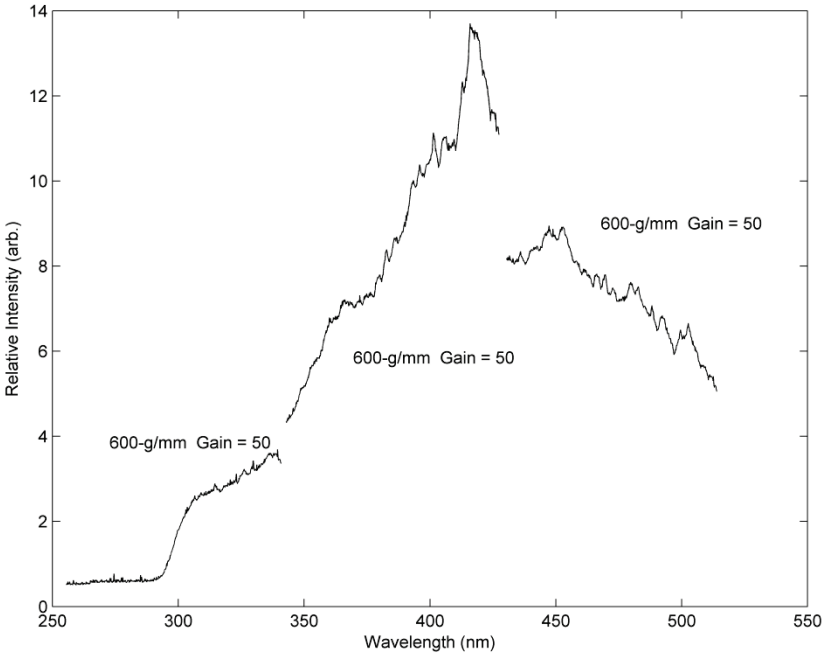

Figure 6.5 These three spectra were obtained using the 600-g/mm grating, which is blazed at 500-nm, and a CCD intensifier gain of 50. Each spectrum is the average of five different breakdowns.

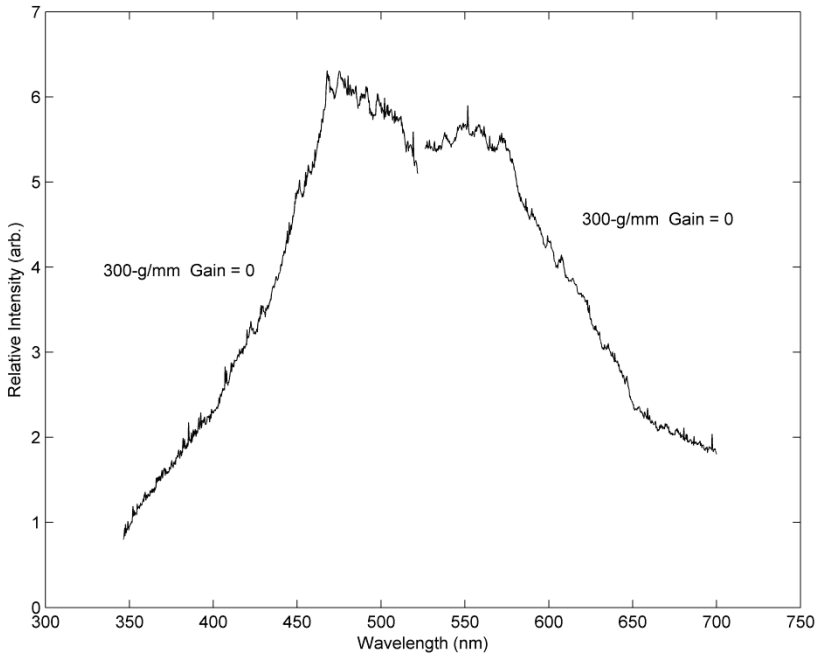

Figure 6.6 These two spectra were obtained using the 300-g/mm grating, which is blazed at 500-nm, and a CCD intensifier gain of 0. Each spectrum is the average of five different breakdowns.

6.3 Calibration Spectra

The calibration data was obtained by transmitting the light from the calibration lamps through the fiber and the CCD. The setup of the grating, center wavelength, and gain was identical to the setup of the raw breakdown spectra. For example, to obtain a calibration spectrum to calibrate the raw data of figure 6.6 centered at 438-nm, the lamp light was transmitted through the fiber and the CCD when the grating was 300-g/mm, the center wavelength was 438-nm, and the gain was set at 0. The following figures are the calibration spectra.

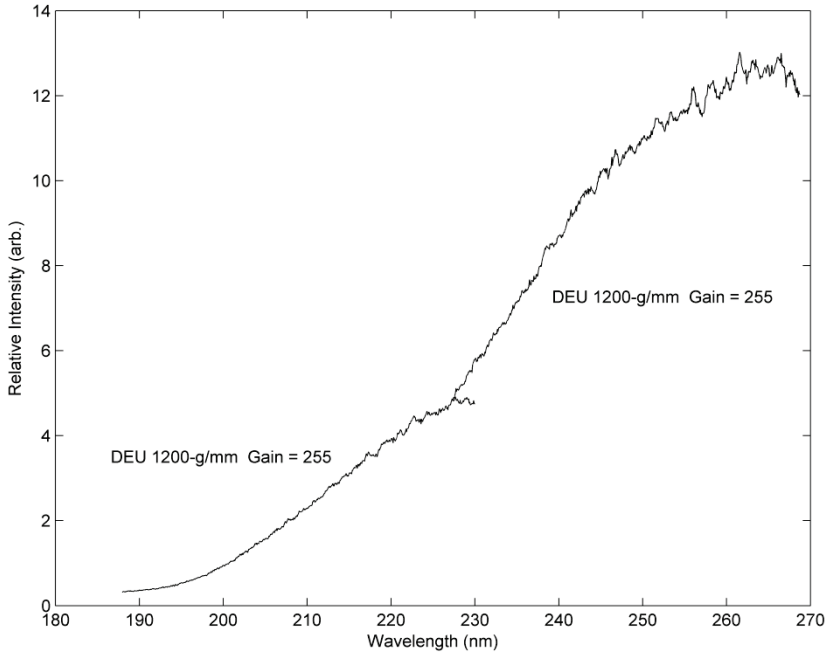

Figure 6.7 These two spectra were obtained using the 1200-g/mm grating, which is blazed at 300-nm, and a CCD intensifier gain of 255. Each spectrum is the light from the deuterium lamp through the fiber and spectrograph.

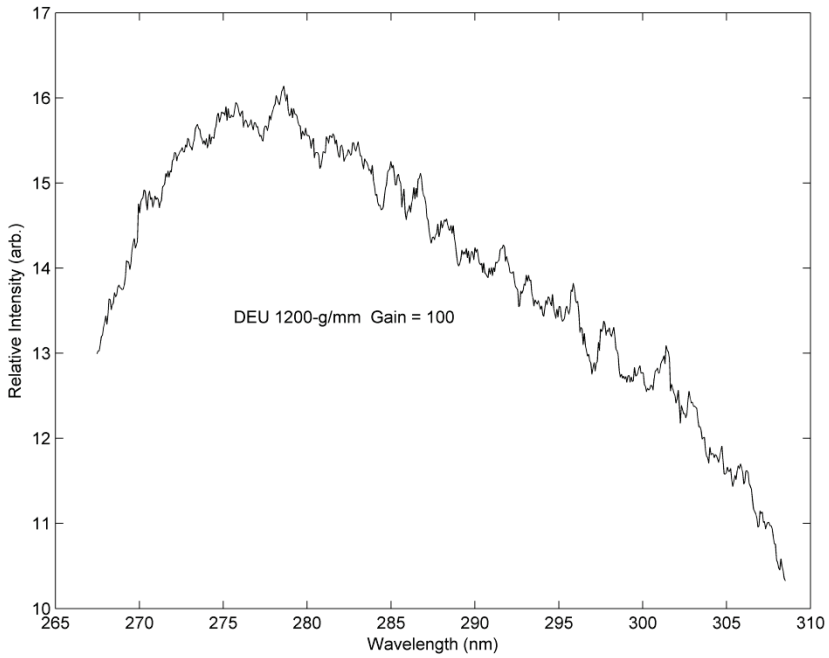

Figure 6.8 This spectrum was obtained using the 1200-g/mm grating, which is blazed at 300-nm, and a CCD intensifier gain of 100. Each spectrum is the light from the deuterium lamp through the fiber and spectrograph.

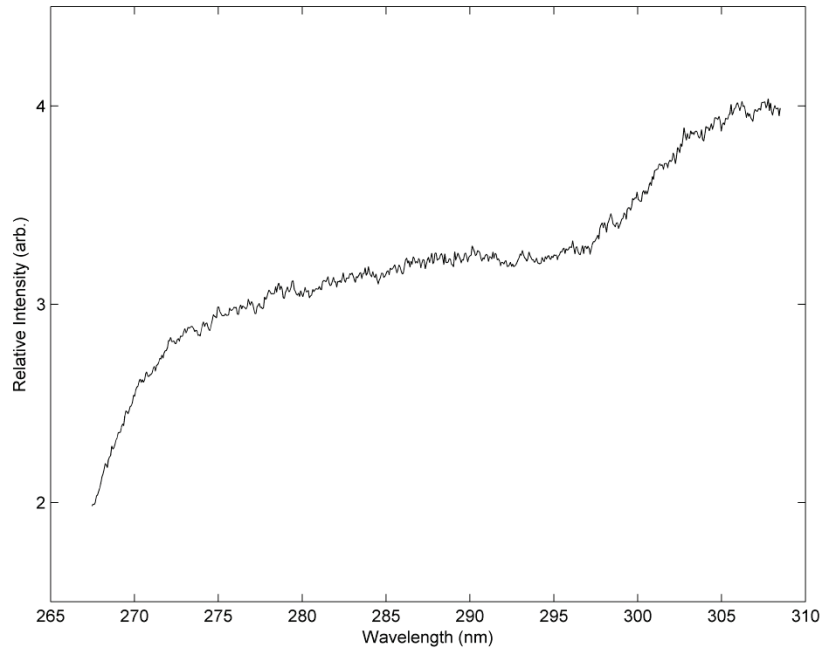

Figure 6.9 This spectrum was obtained using the 1200-g/mm grating, which is blazed at 300-nm, and a CCD intensifier gain of 100. This spectrum is the light from the QTH lamp through the fiber and spectrograph.

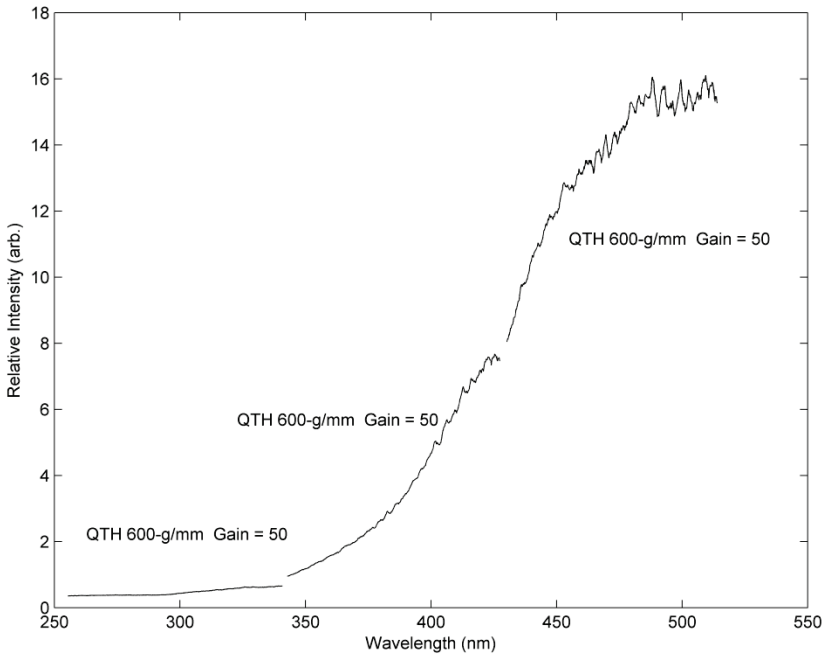

Figure 6.10 These three spectra were obtained using the 600-g/mm grating, which is blazed at 500-nm, and a CCD intensifier gain of 50. Each spectrum is the light from the QTH lamp through the fiber and spectrograph.

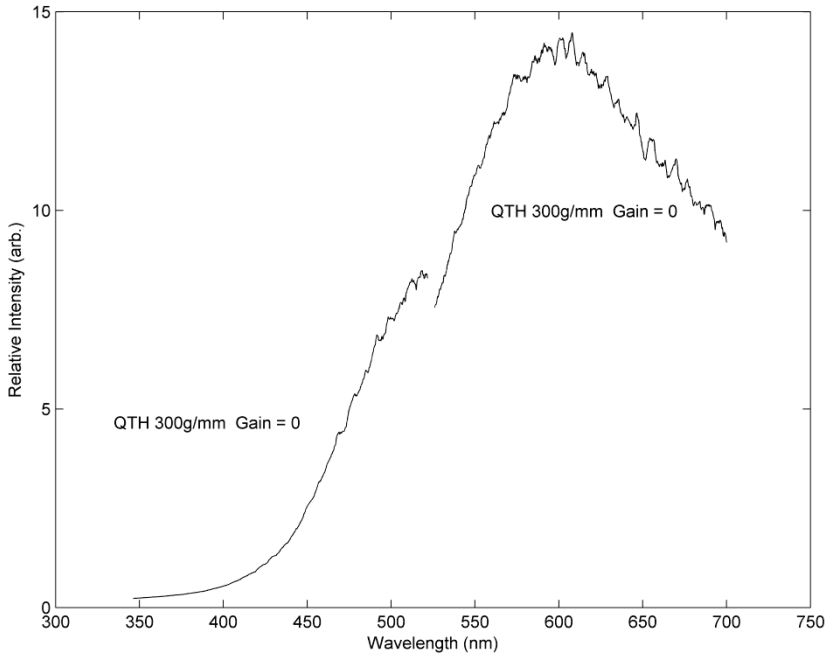

Figure 6.11 These two spectra were obtained using the 300-g/mm grating, which is blazed at 500-nm, and a CCD intensifier gain of 0. Each spectrum is the light from the QTH lamp through the fiber and spectrograph.

6.4 Flat-field Correction Spectrum

A flat-field correction is the last correction applied to the raw breakdown spectra. A flat-field correction is necessary to account for pixel performance variance on the CCD pixel screen. The CCD pixel screen may have bad or dimmer pixels that produce erroneous data. The spectrum for the flat field correction is obtained by dismounting the CCD from the spectrograph and applying a uniform light source to it. In this particular case, the flat-field spectrum was measured by placing a white piece of paper over the entire CCD lens and illuminating that piece of paper from the opposite side with a fluorescent light. This created a uniform light intensity over the surface of the CCD lens. A flat-field spectrum was measured for each of the intensifier gains: 0, 50, 100, and 255. The flat-field for the

gain of zero is shown in figure 6.11. The rest of the flat-field spectra can be found in appendix D.

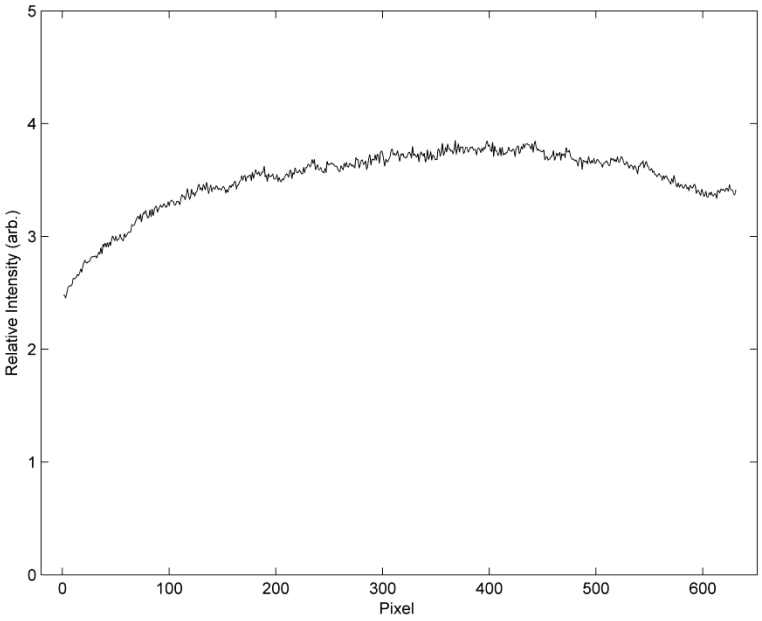

Figure 6.12 This flat-field spectrum was obtained with an intensifier setting of zero. Notice that the x-axis is the pixels across the CCD screen 1-631.

6.5 Calibrated (Actual) Breakdown Spectra

The calibrated (actual) breakdown spectra were obtained by inputting the spectra from figures 6.1 through 6.11 into equation 6.1. The raw data is already averaged, of course, and presented in figures 6.3 to 6.6. The individual spectra for each gain are presented in figures 6.12 to 6.15 and all the spectra a presented together in figure 6.16. These are the true spectrums. In figure 6.11 there appears to be a large increase in intensity as the wavelengths decrease past 220-nm. This is an artifact of the calibration and does not really exist; it is included in figure 6.11 but removed in figure 6.16. The peak results from a division of a number very close to zero in the calibration procedure.

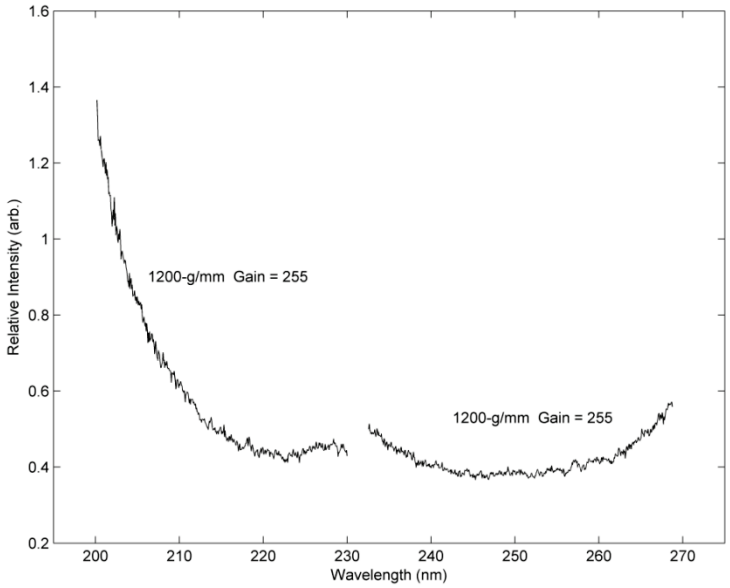

Figure 6.13 These two calibrated breakdown spectra were obtained with the 1200-g/mm grating with a gain of 255. The deuterium lamp was used for the calibration. There appears to be a small peak around 230-nm. The peak on the left side of the graph is an artifact of the limited transmittance at those wavelengths. The calibration forces a division by a number very close to zero, which causes very large numbers to develop.

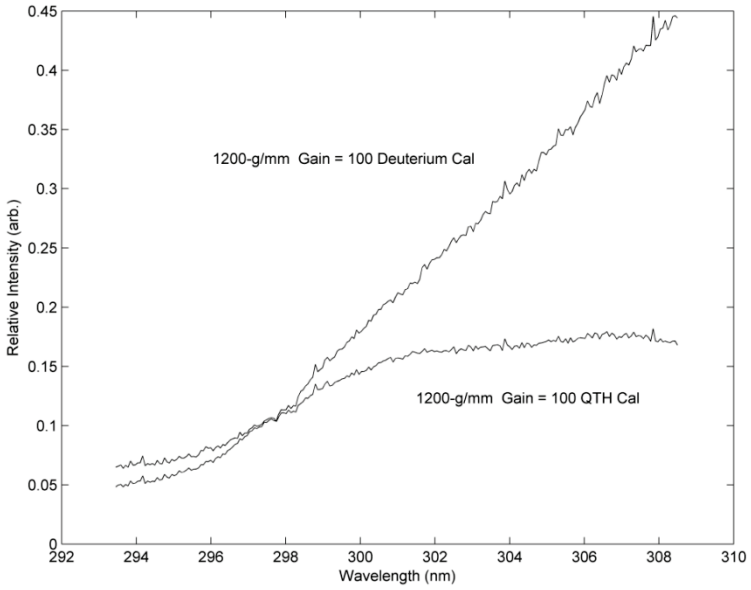

Figure 6.14 These two calibrated spectra were obtained from the 289-nm data with the 1200-g/mm grating and a gain of 100. The spectra were calibrated with the QTH and deuterium lamps, respectively. They both show an increasing intensity towards 310-nm and similar minor peak locations.

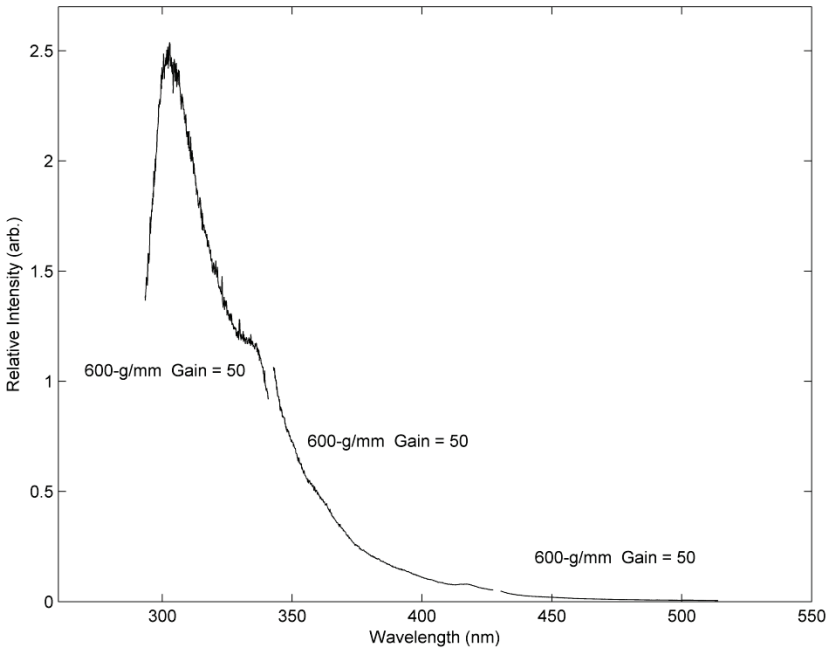

Figure 6.15 These three calibrated spectra were obtained from the 600-g/mm grating and a gain of 50. The spectra show a very pronounced black body peak at around 310-nm and minor peaks at around 340 and 420-nm.

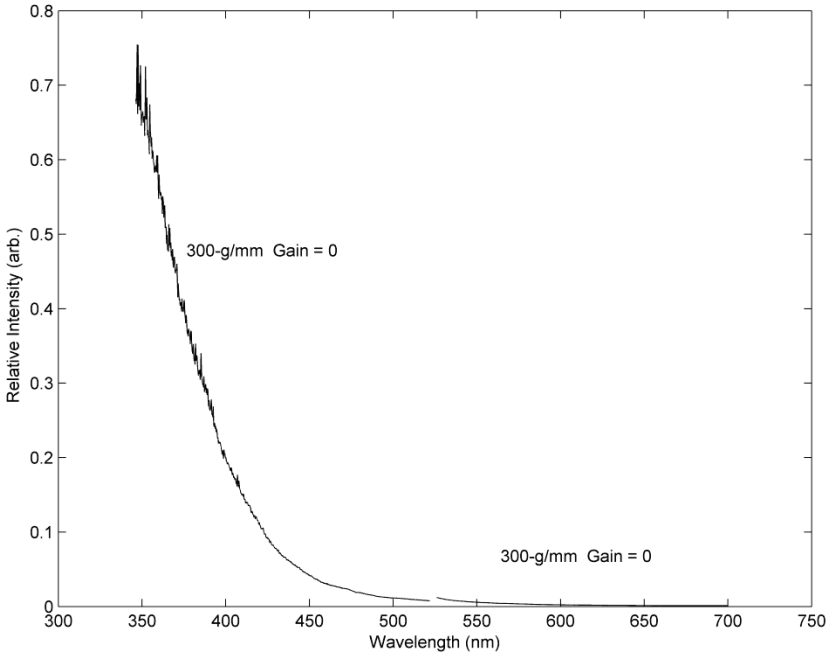

Figure 6.16 These two calibrated spectra were obtained from the 300-g/mm grating and a gain of 50. The spectra show an increasing intensity with decreasing wavelength. This supports the findings of the other gratings.

6.6 Corrected Spectrum

Figure 6.16 shows all the calibrated breakdown spectra on one graph to show how the spectra model a black-body distribution. The distribution peaks between 305 and 315-nm. The erroneous data at the lower wavelengths was removed. A legend is included in the figure to help decipher the spectra. The figure is very large and detailed, so it is included as a landscape orientation on the following page.

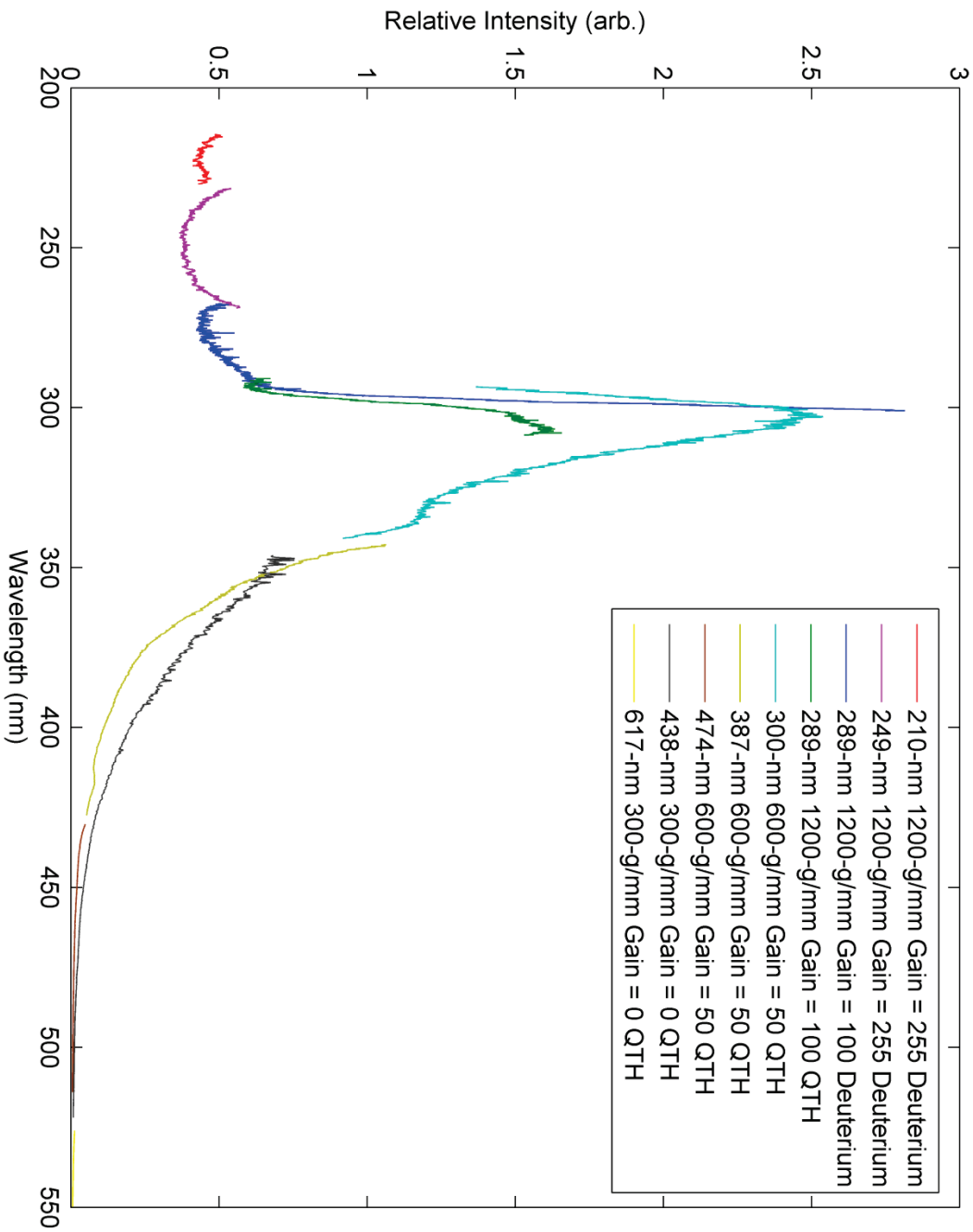

Figure 6.17 This figure compilation of all the spectra. The spectra peak between 305 and 315-nm. The compilation spectrum models the black-body spectra of figure 3.2.

6.7 Black-Body Temperature and Energy Output

The black-body radiation has a maximum photon flux at a certain wavelength, depending on the temperature. The temperature of the breakdown plasma was obtained from equation 3.7. The spectra obtained appear to peak between 305 and 315-nm indicating a plasma temperature between **9206 and 9508-K**, or about 0.9-eV.

Using the Stefan-Boltzmann law, equation 3.8, the energy radiated per unit area per unit time can be obtained, where $\sigma = 5.6704 \times 10^{-8}$ $[Js^{-1}m^{-2}K^{-4}]$ A plasma temperature of 9500 K corresponds to an energy output of **461.86 [MW m^{-2}].** The plasma has been modeled as a perfect black-body with an emissivity of one.

It is important to note that the maximum photon flux around 305-nm falls in the 200 to 380-nm absorption range of the PMMA and the transmission range of the pressurized SF_6 gas. This indicates that there is a large intensity of photon flux incident on the surface of the PMMA possibly contributing to surface charging and flashover discussed in the previous chapters.

Chapter 7: Summary

The overall research objective was to reduce the rate of insulator flashover in the RIMFIRE gas switch utilized by Sandia National Labs in their "Z-Machine" fusion system. A high insulator flashover rate causes lengthy and costly delays as the damaged insulators must be replaced. The UV flux generated by the breakdown plasma was thought to be contributing to undesirable charge accumulation on the surface of the insulator. This charge distribution on the insulator may create voltage gradients across its surface leading to flashover due to secondary electron emission.

In an effort to characterize the breakdown plasma, several spectrographic experiments were performed to investigate the plasma's optical parameters. A timing diagram of the MUTTS electrical system was developed to properly synchronize the ICCD shutter gate with the breakdown current pulse. The absorption and transmission characteristics of the insulator material and the black-body temperature spectrum of the breakdown plasma were recorded. The plasma breakdown spectra presented in this thesis were measured through a fiber optic coupled to an optical multichannel analyzer. The plasma temperature and optical output power are reported for a high voltage 3-MV switch.

Calibration procedures were employed to transform the raw breakdown spectra into the corrected spectra of figure 6.17. The calibration was necessary to correct for transmission inefficiencies in the fiber optic, spectrograph, and ICCD. A Varian Cary50 Spectrophotometer system was used to determine the transmittance and absorption of a

0.5” thick piece of PMMA with three different cleaning procedures. The sample cleaned with hexane shows slightly less transmission when nearing cutoff.

Analysis of the black-body spectrum yields an approximate plasma temperature between **9206 and 9508-K**. This plasma temperature corresponds through the Stefan-Boltzmann law to an energy output of **461.86 [MW m^{-2}]**. Transmittance and absorption tests show that optical flux below 390-nm is absorbed by the PMMA and transmitted by the SF_6 gas, possibly contributing to charge accumulation on the surface of the insulator through photon collision dynamics [1,2,3]. This, in turn, may lead to flashover of the insulator surface.

The plasma temperature is the measure of the thermal kinetic energy of the ambient electrons. Because of their low mass, electrons quickly approach thermal equilibrium leading to a Maxwellian energy distribution. The temperature influences the degree of plasma ionization. An arc discharge is considered thermal plasma that approaches a fully ionized state. High-pressure arc discharges typically have an electron density on the order of $10^{15\text{-}17}/cm^3$ [4].

Another option available to reduce the flashover rate is altering the work function of the surface of the PMMA insulator. It was determined that the photons generated by the breakdown discharge have sufficient intensity and wavelength to generate charge on the surface of the insulator. Changing the work function of the insulator surface (~215-nm) to

a value below the transmission wavelength of the SF_6 (160-nm) would reduce surface charge formation due to minimal photoemission efficiency.

Further experimentation is needed to complete the characterization of the RIMFIRE breakdown plasma. Determining the absorption coefficient of the plasma would allow calculation of the plasma density. Capacitive electrostatic probes placed along the surface of the insulator would allow for direct measurement of the charge accumulation on the surface of the insulator. These measurements coupled with the plasma temperature would help pinpoint the source of insulator flashover.

REFERENCES FOR CHAPTER 7

[26] J. Javedani, T. Houck, D. Lahowe, G. Vogtlin, D. Goerz, “Insulator Surface Flashover due to UV Illumination”, IEEE. Conf. Pulsed Power, 2009.

[27] J.T. Krile, A. Neuber, H. Krompholz, “Effects of UV Illumination on Surface Flashover Under Pulsed Unipolar Excitation”, IEEE Conf. Plasma Sci., 2007.

[28] R. Morrow and T. Blackburn, “The Role of Photoionization in Streamer Discharge Formation in Voids”, IEEE Trans. on Plasma Sci., 1999.

[29] T. Fujimoto, "Plasma Spectroscopy", Oxford Science Publications, 2007.

Appendix A
Local Thermodynamic Equilibrium Considerations

The distribution of electrons within breakdown plasma models a classical Maxwell Distribution,

$$f(v)dv = (\frac{m}{2\pi KT_e})^{\frac{3}{2}} e^{(-\frac{mv^2}{2kT_e})} 4\pi v^2 dv$$

which satisfies the normalization condition,

$$\int f(v)dv = 1$$

with an average electron speed of,

$$\bar{v} = \sqrt{\frac{8KT_e}{\pi m}}$$

and a most probable electron speed of,

$$v_p = \sqrt{\frac{2KT_e}{m}}$$

which has a corresponding energy distribution of,

$$f(E)dE = 2\left(\frac{E}{\pi}\right)^{\frac{1}{2}} (KT_e)^{-\frac{3}{2}} e^{(-\frac{E}{kT_e})} dE$$

and an average energy of,

$$\bar{E} = \frac{3kT_e}{2}$$

In thermodynamic equilibrium the ratio of the number of ions per unit volume in two different energy levels, or population density ratio, is given by the Boltzmann distribution:

$$\frac{n_{z-1}(q)}{n_{z-1}(p)} = \frac{g_{z-1}(q)}{g_{z-1}(p)} \exp\left(-\frac{E_{z-1}(p,q)}{kT_e}\right)$$

where p and q are ionization levels (p < q), n is the population, and g is the statistical weight. This can be rewritten as:

$$\frac{n_z(1,v)}{n_{z-1}(p)} = \frac{g_z(1,v)}{g_{z-1}(p)} \exp\left(-\frac{\Delta E}{kT_e}\right)dv$$

where $n_z(1,v)dv$ and $g_z(1,v)dv$, denote the population and statistical weight, respectively, of the upper level. ΔE is the energy difference between the upper and lower levels:

$$\Delta E = \frac{mv^2}{2} + X_{z-1}(p)$$

where $X_{z-1}(p)$ is the energy separation between the "p" level and the upper continuum levels. Plasma calculations require the use of a six dimensional phase space with three dimensions for the spatial coordinates (x, y, z) and three dimensions for the momentum coordinates (p_x, p_y, p_z). Each cell has an area h. The number of states deriving from the motion of the electrons is:

$$gdv = \frac{\Delta x \Delta p_x}{h} \cdot \frac{\Delta y \Delta p_y}{h} \cdot \frac{\Delta z \Delta p_z}{h}$$

where Δx, Δy, and Δz are the spatial coordinate widths allocated to one of the free electrons and Δp_x, Δp_y, and Δp_z are similarly the momentum coordinate widths. In polar coordinates this equation reduces to:

$$gdv = \frac{4\pi m^3 v^2 dv}{h^3}$$

The statistical weight of the upper level is thus given as:

$$g_z(1,v)dv = \frac{4\pi m^3 v^2 dv}{n_e h^3} g_e g_z(1)$$

After a few further reduction steps and applying the normalization condition for the Maxwell distribution we obtain the Saha-Boltzmann distribution:

$$\frac{n_z(1)n_e}{n_{z-1}(p)} = \frac{2g_z(1)}{g_{z-1}(p)}\left(\frac{2\pi mkT_e}{h^2}\right)^{\frac{3}{2}} exp\left(-\frac{X_{z-1}(p)}{kT_e}\right)$$

or

$$n_{z-1}(p) = Z(p)n_z(1)n_e$$

where Z(p) is called the Saha-Boltzmann coefficient. Under certain conditions, thermodynamic equilibrium may be established in the plasma and the population of the excited level p is given by the Saha-Boltzmann distribution equation. If this is the case, we can say that level p is in local thermodynamic (LTE) with respect to ion z. In the case that the LTE population extends down to the ground state p = 1, this situation is defined as complete local thermodynamic equilibrium. It is assumed that the light radiated by the breakdown plasma in RIMFIRE is isotropic and maintains approximately constant intensity over the line profile of the transition.

Appendix B
PMMA Transmission and Absorption Graphs

The seven graphs obtained from the Varian Cary50 Spectrophotometer are shown below. The nine samples were pieces of the PMMA insulator material that was 0.5-cm in depth. These measurements were useful in determining the transmittance and absorption of the PMMA. Three cleaning procedures were used: no cleaning (A), hexane (B), and Windex (C). Hexane was found to have slightly more absorption and slightly less transmittance when at cutoff. The last figure is an anomaly found at 225-nm where there appears to be slight transmittance.

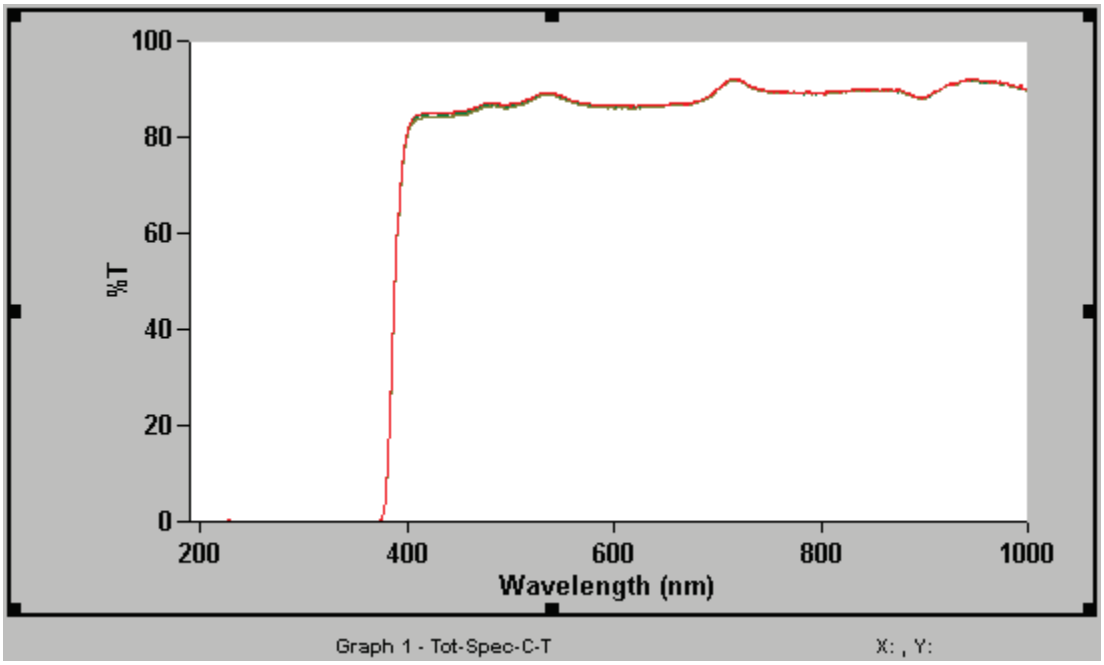

Figure B.1 Transmittance of light through PMMA from 200 to 1000-nm of samples 1-3.

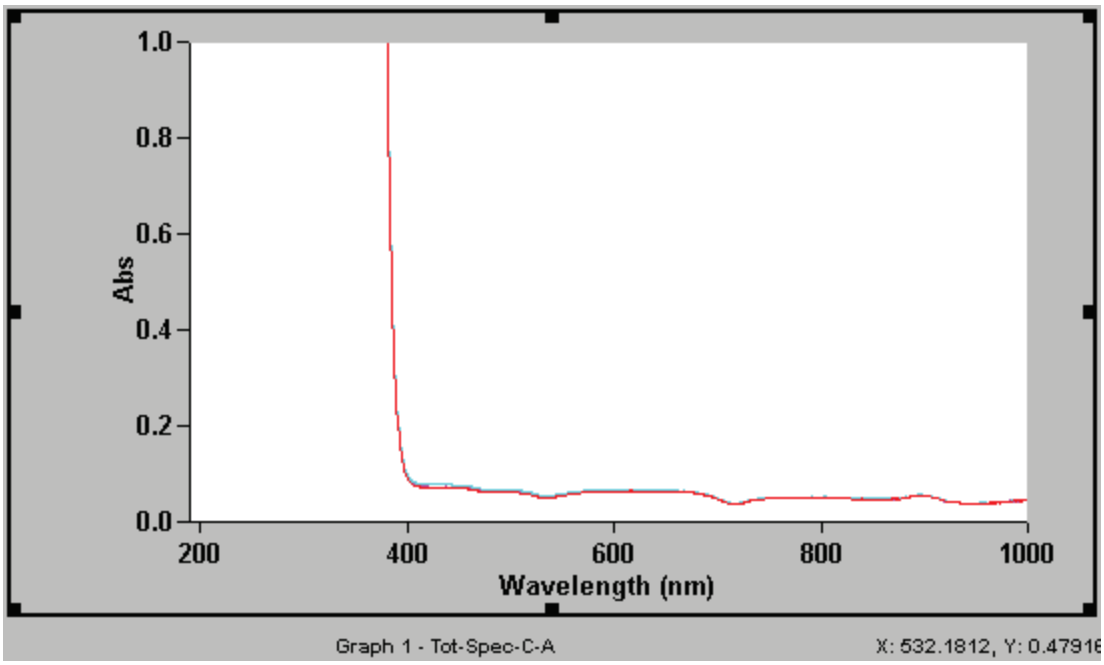

Figure B.2 Absorption of light by PMMA from 200 to 1000-nm of samples 1-3.

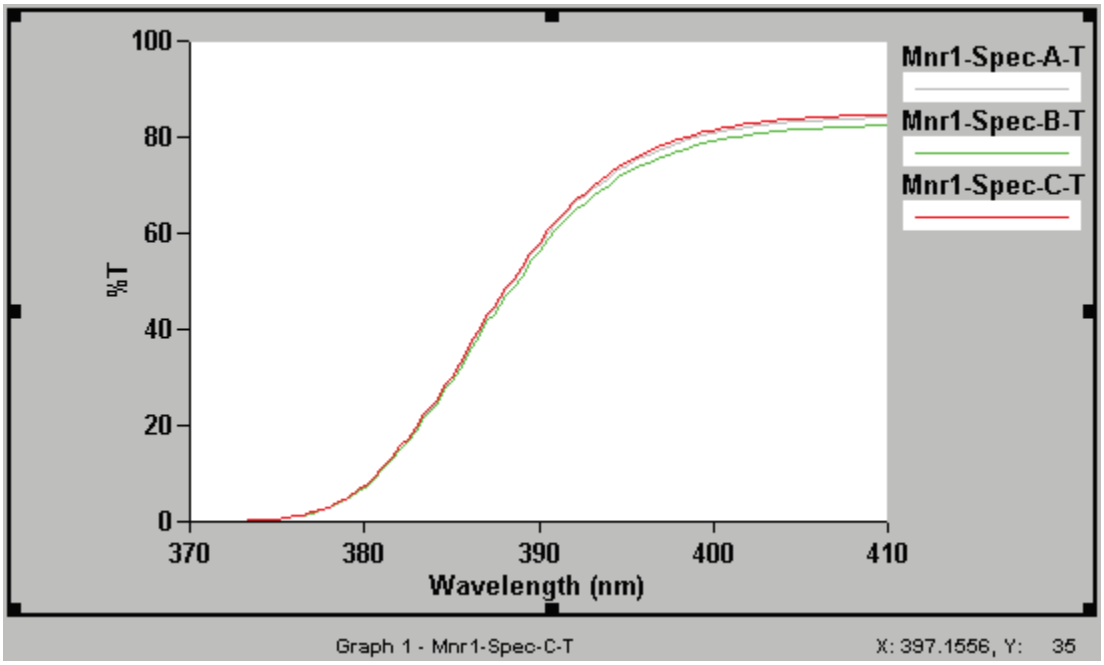

Figure B.3 Transmission of light through PMMA from 370 to 410-nm of samples 4-6.

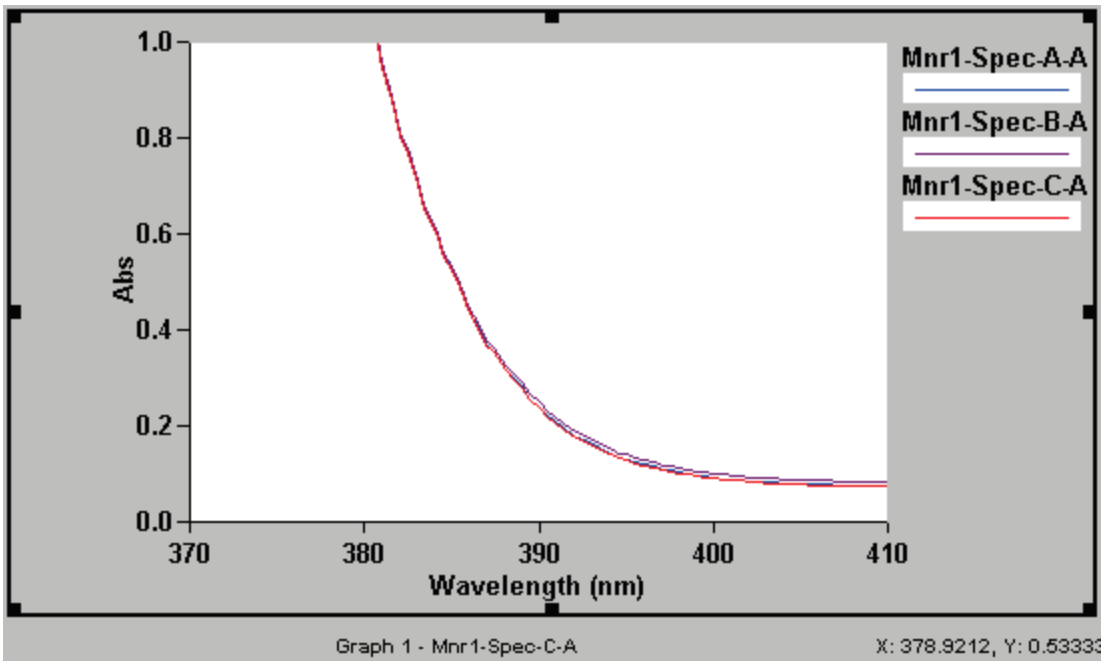

Figure B.4 Absorption of light by PMMA from 370 to 410-nm of samples 4-6.

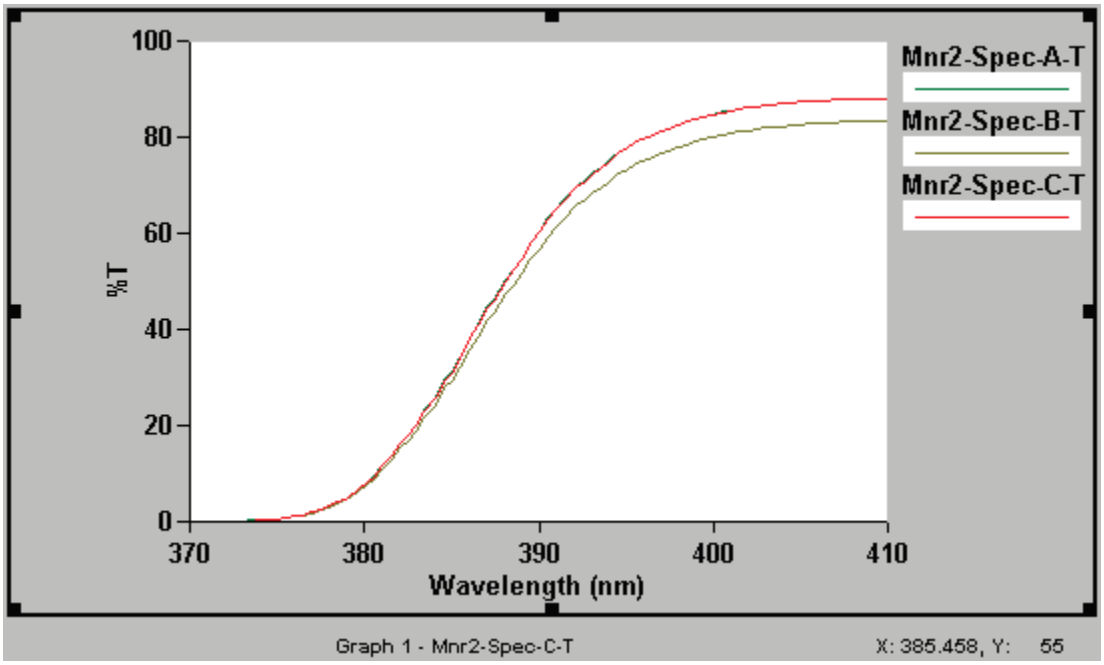

Figure B.5 Transmittance of light through PMMA from 370 to 410-nm of samples 7-9

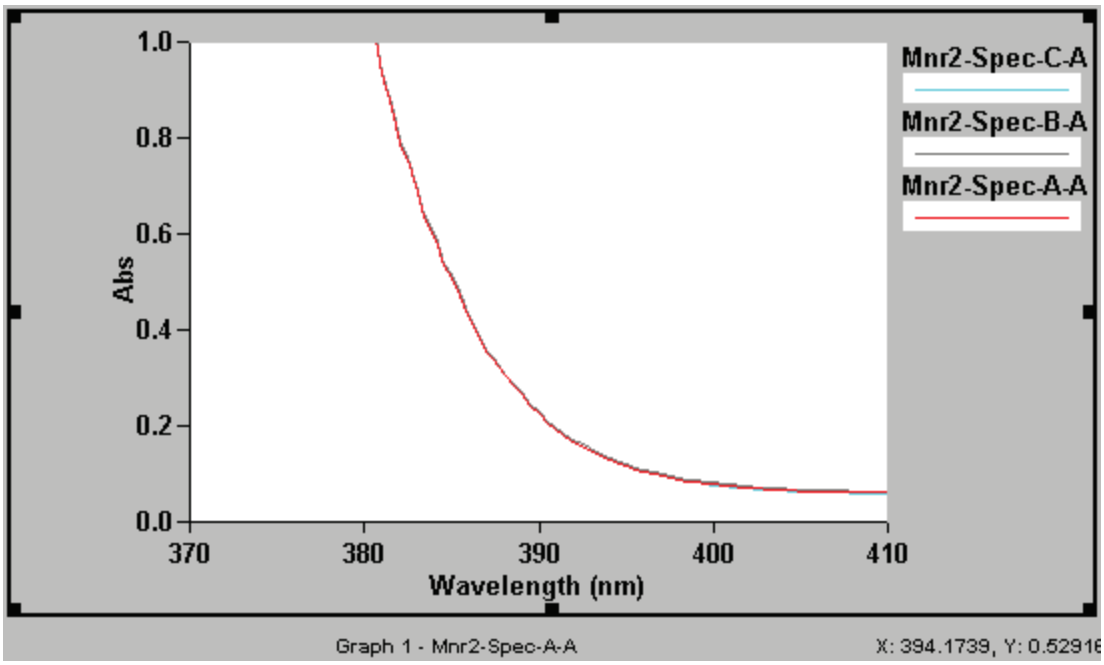

Figure B.6 Absorption of light by PMMA from 370 to 410-nm of samples 7-9.

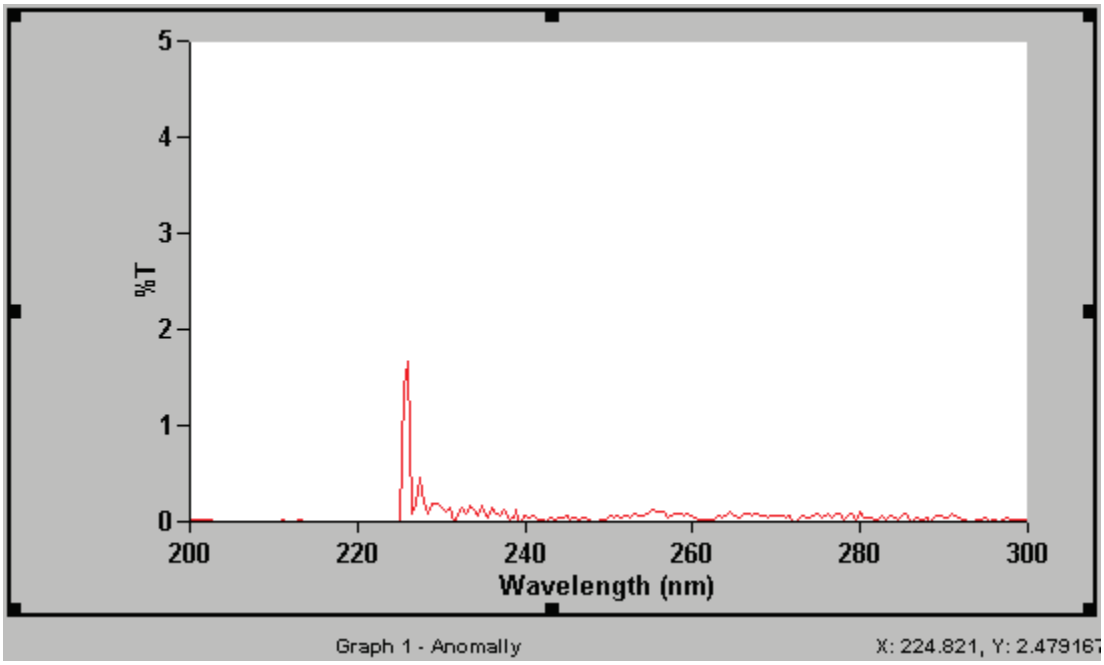

Figure B.7 Transmission of light at 225-nm validated by repeated tests with several samples.

Appendix C
Calibration Lamp Output Equation

$$\boldsymbol{Irradiance}\frac{(\boldsymbol{mW})}{\boldsymbol{m^2(nm)}} = \lambda^{-5} \times \exp\left(\mathrm{A} + \frac{\mathrm{B}}{\lambda}\right) \times (\mathrm{C} + \frac{\mathrm{D}}{\lambda} + \frac{\mathrm{E}}{\lambda^2} + \frac{\mathrm{F}}{\lambda^3} + \frac{\mathrm{G}}{\lambda^4} + \frac{\mathrm{H}}{\lambda^5})$$

Deuterium Lamp Coefficients
A=28.177816
B=-292.916972
C=10.011787
D=-8926.710041
E=3005525.040991
F=-400242020.780274
G=16696966118.893990
H=0.000000000000000

QTH Lamp Coefficients
A=43.0959860542114
B=-4516.37542690325
C=0.994468962389889
D=-6.10016686518227
E=24681.5682111474
F=-13030724.124835
G=722349437.17521
H=0.000000000000000

Appendix D

Flat-Field Spectra

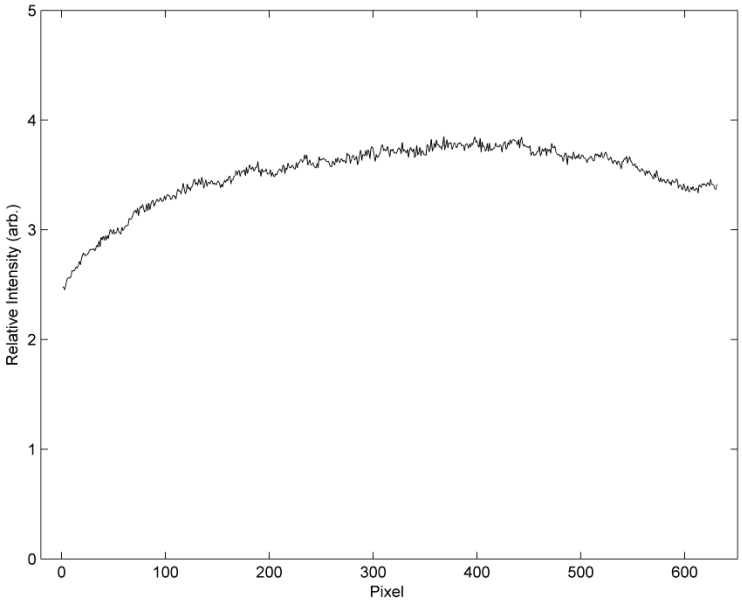

Figure D.1 Flat-field spectrum at a gain of 0.

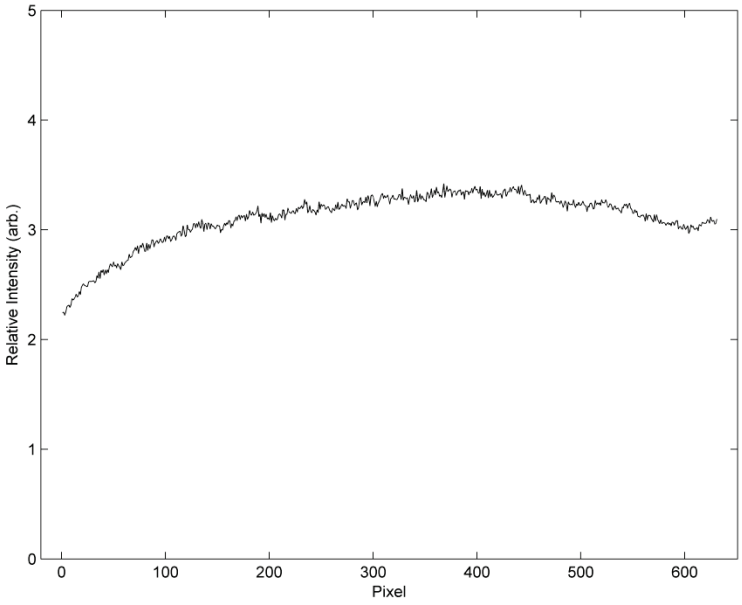

Figure D.2 Flat-field spectrum at a gain of 50.

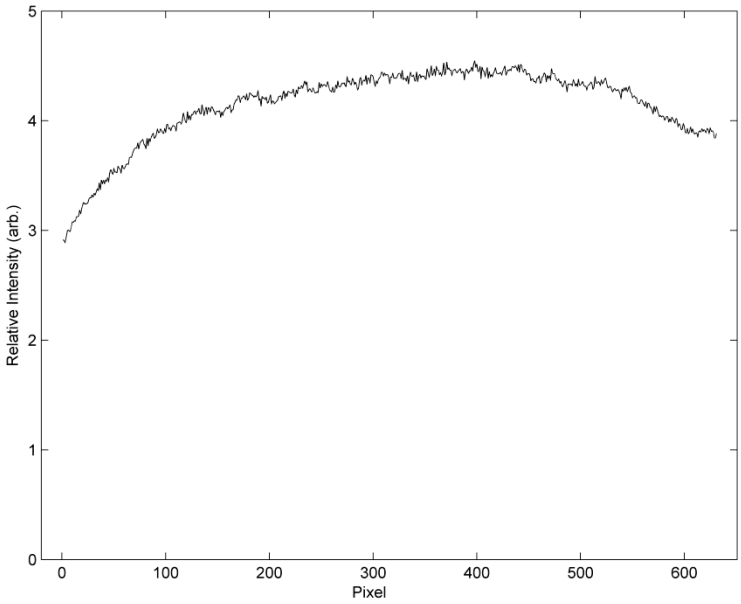

Figure D.3 Flat-field spectrum at a gain of 100.

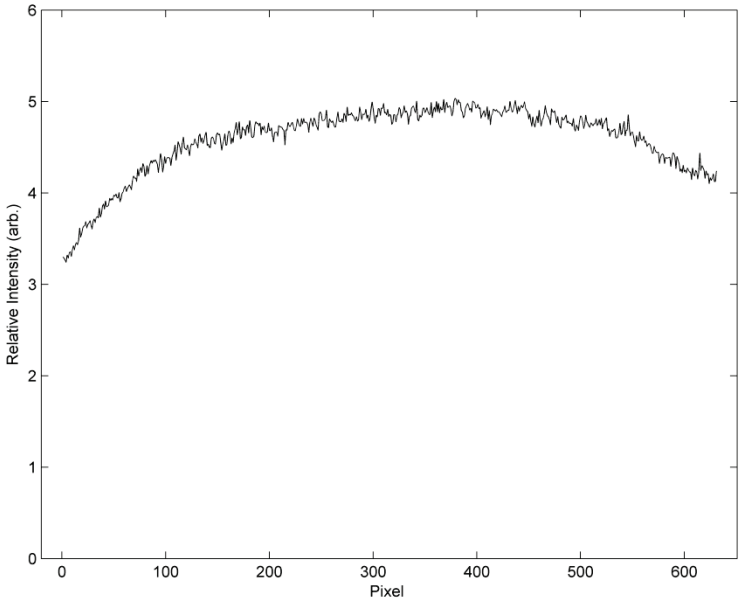

Figure D.4 Flat-field spectrum at a gain of 255.